# Birnaviral Hijacking of Endosomal Membranes

Flavia A. Zanetti[a,#], Ignacio Fernández[b,#]; Eduard Baquero[b]; Pablo Guardado-Calvo[b]; Sarah Dubois[c]; Etienne Morel[c]; Victoria Alfonso[d]; Milton O. Aguilera[e]; María E. Celayes[e]; Luis M. Polo[e]; Laila Suhaiman[f,†]; Vanesa V. Galassi[f,g]; María V. Chiarpotti[f,g]; Carolina Allende[h]; Javier M. Rodríguez[h]; José R. Castón[h]; Diego Lijavetzky[i]; Oscar Taboga[d]; María I. Colombo[e]; Mario G. Del Pópolo[f,g]; Félix A. Rey[b]; Laura R. Delgui[e,g,*]

[a] Instituto de Ciencia y Tecnología "Dr. Cesar Milstein", Consejo Nacional de Investigaciones Científicas y Técnicas (CONICET), Saladillo 2468 C1440FFX, Ciudad Autónoma de Buenos Aires, Argentina.

[b] Institut Pasteur, Université Paris Cité, Structural Virology Unit, 25-28 Rue du Dr. Roux, 75015 Paris, France.

[c] Université Paris Cité, INSERM UMR-S1151, CNRS UMR-S8253, Institut Necker Enfants Malades, Rue de Vaugirard 156, 75015 Paris, France.

[d] Instituto de Agrobiotecnología y Biología Molecular (IABIMO), Instituto Nacional de Tecnología Agropecuaria (INTA), Consejo Nacional de Investigaciones Científicas y Técnicas (CONICET), De los Reseros y N. Repetto s/n, Hurlingham B1686IGC, Buenos Aires, Argentina.

[e] Instituto de Histología y Embriología de Mendoza, Universidad Nacional de Cuyo (UNCuyo), Consejo Nacional de Investigaciones Científicas y Técnicas (CONICET), Centro Universitario M5502JMA, 5500 Mendoza, Argentina.

[f] Instituto Interdisciplinario de Ciencias Básicas (ICB), Consejo Nacional de Investigaciones Científicas y Técnicas (CONICET), Padre Contreras 1300, 5500 Mendoza, Argentina.

[g] Facultad de Ciencias Exactas y Naturales, Universidad Nacional de Cuyo (UNCuyo), Padre Contreras 1300, 5500 Mendoza, Argentina.

[h] Department of Structure of Macromolecules, Centro Nacional de Biotecnología (CNB-CSIC), C. Darwin, 3, 28049 Madrid, Spain.

[i] Instituto de Biología Agrícola de Mendoza, Universidad Nacional de Cuyo (UNCuyo), Consejo Nacional de Investigaciones Científicas y Técnicas (CONICET), Almirante Brown 500, M5528AHB. Chacras de Coria, Mendoza, Argentina.

[#]F.A.Z. and I.F. contributed equally to this work.

†Current affiliation: Instituto de Medicina y Biología Experimental de Cuyo (IMBECU) - Consejo Nacional de Investigaciones Científicas y Técnicas (CONICET), Facultad de Ciencias Médicas, Universidad Nacional de Cuyo (UNCuyo), Mendoza, Argentina.

*Laura R. Delgui

**Email:** ldelgui@mendoza-conicet.gob.ar; ldelgui@fcm.uncu.edu.ar

**Author Contributions:** I.F., E.B., F.A.R., M.G.D.P. and L.R.D. designed research; F.A.Z., P.G.C., S.D., E.M., V.A., M.O.A., M.E.C., L.M.P., L.S., V.V.G., M.V.C., C.A., J.M.R., and L.R.D. performed research; I.F., E.B., M.O.A., D.L., M.G.D.P., F.A.R., and L.R.D. analyzed data; J.R.C., O.T., M.I.C. and F.A.R. contributed new reagents/analytic tools; and L.R.D. and M.G.D.P. wrote the paper.

**Competing Interest Statement:** The authors declare no competing interest.

**Keywords:** Birnavirus – Endosomes – Membrane - Phosphatidylinositol-3-phosphate – Replication – Viral evolution.

## Abstract

Birnaviruses form a distinct class of double-stranded RNA (dsRNA) viruses characterized by the absence of a transcription-competent inner core particle. The early endosomes (EE) of cells infected with the infectious bursal disease virus (IBDV) - a prototypical birnavirus and an important avian pathogen - constitute a platform for viral replication. Here, we study the mechanism of birnaviral hijacking of EE membranes for this process. We demonstrate that the viral protein 3 (VP3) specifically binds to phosphatidylinositol-3-phosphate (PI3P) present in EE membranes. We identify the domain of VP3 involved in PI3P-binding and its role in viral replication. Finally, our molecular simulations results unveil a two-stage modular mechanism for VP3 association with EE. Firstly, the carboxy-terminal region of VP3 adsorbs to the membrane via non-specific electrostatic interactions. Then, in the second stage, the VP3 core seals the membrane engagement by specifically binding PI3P through its P2 domain, additionally promoting PI3P accumulation.

## Significance Statement

Birnaviruses are different from the rest of the dsRNA viruses. They contain an RNA-dependent RNA polymerase (RdRp) with a unique motif arrangement in the palm subdomain, their viral particles lack the inner protein layer protecting the dsRNA, and the viral capsid protein VP2 presents a jelly-roll topology characteristic of +sRNA viruses. Here, we provide evidence that birnaviruses replicate in association with cellular membranes. Since the remodeling of the host's membranes is a characteristic shared by all +sRNA viruses, our results highlight parallels in the replication strategy of these "*non-canonical*" dsRNA viruses and +sRNA viruses.

## Introduction

Birnaviruses belong to the *Birnaviridae* family composed of nonenveloped icosahedral dsRNA viruses that infect a wide range of vertebrate and invertebrate hosts. The prototypical and best-characterized family member, IBDV, is the causative agent of Gumboro disease, a highly contagious immunosuppressive disease that affects young chickens (*Gallus gallus*) causing significant damage to the poultry industry (Delmas et al., 2019).

Birnaviruses are unconventional dsRNA viruses, as the virions lack a "*core",* i.e., an inner protein layer containing the genome, which instead forms a filamentous ribonucleoprotein complex (RNP) with the multifunctional protein VP3, the RdRp VP1, and the dsRNA genome segments (Luque et al., 2009b). IBDV contains a single ~70-nm diameter T = 13*l* icosahedral capsid surrounding a polyploid bipartite dsRNA genome (segments A and B, 3.2 and 2.8 kbp, respectively) (Luque et al., 2009a). The X-ray crystal structure of its capsid revealed that VP2 is the only component. VP2 has two main domains, a "shell" domain homologous to the coat proteins of +sRNA such as the T = 3 nodaviruses, and a "tower" domain like those present in the T = 13 middle-layer protein of dsRNA viruses of the order *Reovirales* (Coulibaly et al., 2005). VP3 is a 257-residues long polypeptide with multiple essential roles during the viral life cycle. In the mature virion, VP3 is a component of the RNPs where it is associated with the dsRNA (Luque et al., 2009b). During viral assembly, VP3 acts as a scaffold protein via electrostatic interactions between basic residues of pVP2 and acidic residues at the VP3 carboxy-terminal (Ct) region (Saugar et al., 2010). Additionally, VP3 interacts with VP1 (Lombardo et al., 1999). VP3's multifunctional properties might be mediated by its capacity to form oligomers (Casañas et al., 2008), or by its intrinsically disordered regions. The X-ray crystal structure of the central region of the IBDV VP3 (residues 82 to 222) showed that it consists entirely of α-helices connected by loops that can be divided

into two structural domains linked by a flexible hinge (Casañas et al., 2008). The 36 Ct residues of the protein, a highly hydrophilic region rich in charged amino acids and proline residues, were predicted to be disordered, so it was excluded from the crystallized construct (Casañas et al., 2008). The 81 amino-terminal (Nt) region of VP3 was cleaved during the crystallization process and was absent in the crystal (Casañas et al., 2008). The X-ray crystal structure indicated the presence of two positively charged domains, termed Patch 1 (P1) and Patch 2 (P2) (Valli et al., 2012). Both patches are composed of four discontinuous, positively charged residues forming two exposed patches on the surface of the protein. P1 was demonstrated to be involved in the dsRNA binding-activity of VP3 (Valli et al., 2012).

Previous studies on the subcellular localization of the IBDV replication complex (RC) have shown that IBDV replication components are localized to EE (8). Further analysis revealed that VP3 associates with the cytosolic leaflet of EE membranes via P2, with a critical functional role in the virus life cycle (9). Additionally, the presence of PI3P in EE membranes was demonstrated to be a key host factor for VP3 association and the consequent establishment of IBDV RCs on EE membranes (10).

Here we studied the mechanism mediating the birnaviral hijacking of EE membranes, focusing on the VP3-PI3P interaction. Using biophysical approaches in cell-free *in vitro* systems, we demonstrate that PI3P constitutes the cellular partner for VP3 association to EE membranes. By introducing charge-reversal point mutations on VP3 P2, we established the contribution of each of the four positively charged residues composing P2, with a key role of the arginine at position 200 ($R_{200}$), a residue conserved across all known birnaviruses. Using a reverse genetic system for IBDV, we show that mutating $R_{200}$ abolishes viral replication. Finally, by using molecular simulations, we unveil a potential two-stage modular mechanism for VP3 association with EE. We show that, in the first step, the Ct flexible tail of VP3 adsorbs to the membrane by electrostatic interactions due to its positive charge. Then, in the second stage,

the VP3 core seals the membrane engagement by recruiting PI3P scattered in the EE membrane to the P2 region, promoting a stable VP3-PI3P interaction.

## Results

**Biophysical characterization of VP3 binding to PI3P**. We set up a liposome co-flotation assay to assess the binding of VP3 to PI3P in membranes. We expressed and purified His-tagged VP3 full-length (His-VP3 FL) and confirmed its identity by Western blot using specific anti-VP3 and anti-His antibodies, as well as by mass spectrometry (*SI Appendix*, Fig. S1). We prepared two populations: "liposomes PI3P(-)" and "liposomes PI3P(+)". We confirmed that these preparations were suitable for evaluating the interaction with PI3P by monitoring co-flotation of a recombinant His-2xFYVE domain (Fab1p, YOTB, Vac1p, and EEA1), followed by immunoblot detection of the His-tag (**Fig. 1A**). We observed specific binding of His-VP3 FL to liposomes PI3P(+), evidenced by a significant difference in the ability to bind to both liposome populations (**Fig. 1B**). To further test His-VP3 FL PI3P-binding specificity, we performed a co-flotation assay using liposomes where PI3P was replaced by a different anionic lipid, such as 1,2-dioleoyl-sn-glycero-3-phosphate ("liposomes PA") or [1,2-dioleoyl-sn-glycero-3-phospho-(1'-myo-inositol)] ("liposomes PI") at the same molar ratio. We observed that His-VP3 FL bound to liposomes PI3P(+), but not to liposomes PA or PI, reinforcing the notion that the interaction of VP3 with PI3P is specific (*SI Appendix*, Fig. S2).

Two additional biophysical approaches were implemented. On one side, we prepared liposomes PI3P(-) and PI3P(+), and incubated them with His-2xFYVE or His-VP3 FL that had been pre-bound to Ni-NTA [nickel (II) nitrilotriacetic acid] gold particles. Subsequently we inspected the preparations by cryo-electron microscopy (cryo-EM). We observed gold particles decorating liposomes PI3P(+) in the

presence of both, His-2xFYVE and His-VP3 FL (**Fig. 1C**). On the other side, we performed bio-layer interferometry (BLI) experiments using purified His-VP3 FL, and liposomes PI3P(-) and PI3P(+) (Shah et al., 2014). In the BLI experiments, the protein is immobilized on the tip of Ni-NTA sensors while the liposomes remain in solution, allowing to monitor the molecular interactions in real-time (Kairys et al., 2019). Purified His-Streptavidin and His-2xFYVE were used as negative and positive controls, respectively. A specific liposome PI3P(+) dose-dependent binding of His-2xFYVE and His-VP3 FL was observed (**Fig. 1D**).

Previous studies indicated that the P2 is responsible for PI3P binding on EE membranes (Gimenez et al., 2020, 2018). Yet the Ct region of VP3 is also highly enriched in positively charged residues. We generated a computational model of FL VP3 using AlphaFold2 (Jumper et al., 2021), which predicted a disordered Ct region (pLDTT of 42.6) (**Fig. 1E**). Thus, we hypothesized that both conditions, the positive electrostatic surface charge and the disordered character of the VP3 Ct, might be required for the binding to the surface of EE. To test this hypothesis, we made a VP3 construct bearing a Ct truncation (His-VP3 ΔCt) and used in co-flotation assays and BLI experiments. We did not detect interaction of this mutant with PI3P(-) nor PI3P(+) liposomes (**Fig. 1F, G**). Taken together, our results strongly validate the role of PI3P in the interaction with VP3 and underscore the significance of the Ct domain in mediating this interaction.

**Role of VP3 P2 in the association of VP3 with the EE membrane.** Inspection of the VP3 crystal structure showed that P2 residues ($K_{157}$, $R_{159}$, $H_{198}$ and $R_{200}$) form a positive-charged groove on the protein surface (**Fig. 2A-B**). We prepared VP3 point mutants with reversed charge in a pcDNA vector backbone, giving rise to pcDNA VP3 $K_{157}D$, $R_{159}D$, $H_{198}D$ and $R_{200}D$. The calculated electrostatic potential of P2 for each of these mutants is shown in **Fig. 2C**. Firstly, we used QM7 cells transiently

overexpressing VP3 P2 Wild Type (WT), P2 (all reversed) or the four single mutation of P2 to quantitatively assess their cellular distribution. We observed a punctuated distribution of VP3 P2 WT, $K_{157}D$, $R_{159}D$ and $H_{198}D$. In contrast, the specific indirect immunofluorescence (IIF) signal of VP3 P2 all reversed and $R_{200}D$ showed a diffuse cytosolic distribution (**Fig. 2D, panels framed in red**). Secondly, we assessed the distribution of the VP3 constructs in QM7 cells transiently overexpressing EGFP-Rab5. Rab5 regulates the homotypic tethering and fusion of EEs, and it is considered a genuine marker of EEs (Gorvel et al., 1991). As observed in **Fig. 2E**, and the quantitative colocalization analysis (*SI Appendix*, Fig. S3), VP3 P2 WT, $K_{157}D$, $R_{159}D$ and $H_{198}D$ showed a marked colocalization with EGFP-Rab5. In contrast, the VP3 P2 all reversed and $R_{200}D$-derived IIF signal indicated a cytosolic distribution (**Fig. 2E, panels framed in red)**. Taken together, these results strongly suggest that $R_{200}$ in the P2 patch bears a critical role in the association of VP3 with EE membranes.

**Role of VP3 P2 in the association of VP3 with PI3P on the EE membrane.** To further assess the contribution of P2 residues to for PI3P binding by VP3, we set up two additional cell biology assays. One consists of co-transfecting cells with EGFP-2xFYVE and VP3 constructs, and detecting them by confocal laser scanning microscopy (CLSM). The second one consists of assessing the ability of purified GST-2xFYVE, which recognizes endogenous PI3P, to co-localize with VP3. We employed QM7 cells transiently co-overexpressing EGFP-2xFYVE and VP3 P2 WT, P2 all reversed, or the four point mutants to evaluate their colocalization. As shown in **Fig. 3A**, we observed a punctuated distribution with a marked co-localization with EGFP-2xFYVE for VP3 P2 WT while for VP3 P2 all reversed the IIF signal indicated a cytosolic distribution of the protein with the loss of colocalization with EGFP-2xFYVE (**Fig. 3A, red framed panels on the upper two rows**). Regarding the point mutants, we observed a loss of punctuated distribution and EGFP-2xFYVE co-localization for VP3 FL $R_{200}D$ (**Fig. 3A, red framed**

**panels on the bottom row**). Then, we used the GST-2xFYVE purified domain to recognize endogenous PI3P in fixed cells (Nascimbeni et al., 2017). GST-2xFYVE was used as the "primary antibody", which was labelled with a fluorescent anti-GST antibody. As an additional control in these experiments, we immunostained the EE with antibodies anti-EEA1. As shown in **Fig. 3B**, VP3 P2 WT demonstrated a conspicuous PI3P-bearing EEA1 positive endosomes location. In addition, we observed a similar distribution for VP3 $K_{157D}$, $R_{159}D$, and $H_{198}D$ and a drastic change in VP3 FL $R_{200}D$ mutant, which appeared utterly cytosolic, losing its capacity to bind to PI3P-bearing EE membranes (**Fig. 3B, red framed panel on the lowest row**). These results provide additional support to $R_{200}$ as being essential for this interaction.

**VP3 $R_{200}$ is crucial for binding to PI3P.** To confirm the role of $R_{200}$ in binding to PI3P-bearing EE, we devised a liposome co-flotation assay using a recombinant His-tagged $R_{200}D$ VP3 mutant. When assayed in parallel with His-2xFYVE and His-VP3 FL, we observed that His-VP3 FL $R_{200}D$ lost binding to PI3P(+) liposomes (**Fig. 4A**). To confirm that the lack of binding was not due to misfolding of the mutant, we compared the circular dichroism spectra of mutant and WT proteins, without detecting significant differences (**Fig. 4B**). To assess its relevance in IBDV infectivity, we generated recombinant mutant IBDV by reverse genetics. QM7 cells were transfected with the plasmids SegA, SegB or Seg.$R_{200}D$ alone (as controls) or with a mixture of plasmids SegA+SegB or SegA.$R_{200}D$+SegB. At 8 h post transfection (p.t.) the cells were recovered and re-plated onto fresh non-transfected cells. At 72 h post-plating, the generation of foci forming units (FFUs) was revealed by Coomassie staining. As expected, single-transfections of SegA, SegB or Seg.$R_{200}D$ did not produce FFUs. As observed in **Fig. 4C**, the transfection of SegA+SegB produced detectable FFUs while no FFUs were detected after the transfection of SegA.$R_{200}D$+SegB (**Fig. 4C**). Given the relevance of VP3 $R_{200}$, we assessed its conservation among

members of the *Birnaviridae* family. For this, a multiple sequence alignment of VP3 reference sequences was performed (*SI Appendix*, Fig. S4A). As shown, IBDV VP3 has 32-39% identity to the other selected homologues (*SI Appendix*, Fig. S4B). A closer look at the VP3 P2 revealed the complete conservation of $R_{200}$ (**Fig. 4D**). Taken together, these findings show that VP3 $R_{200}$ plays an important role mediating the VP3-PI3P interaction, highlighting the active participation of EE membranes during the infectious cycle of birnaviruses.

**Electrostatic forces mediate VP3 membrane binding.** Computer simulations based on coarse-grain models were designed to assess the binding free-energy and adsorption mechanism of three protein variants: VP3 Ct, VP3 ΔNt, and VP3 FL. The VP3 Ct region, with a positive electrostatic charge of +5, was modeled as an intrinsically disordered region according to the AlphaFold2 prediction (**Fig. 1E**). VP3 ΔNt encompasses residues 82 to 257 and is electroneutral. This variant was chosen primarily because it retains the structural data from the crystallized protein. Similarly to His-VP3 FL, His-VP3 ΔNt retains the ability to bind to liposomes PI3P(+) (see *SI Appendix*, Fig. S5A-C). Finally, VP3 FL is the full length monomeric VP3, using the AlphaFold2 predicted structure with an overall electrostatic charge of -3. We employed the Molecular Theory (MT) approach to obtain adsorption free-energy profiles, PMF(z), at different salt concentrations (Chiarpotti et al., 2021; Ramírez et al., 2019). **Figure 5** (panels A-C) shows PMF(z), where z represents the distance between the center of mass of the protein and the center of the membrane, at 50 and 150 mM NaCl. As observed in **Fig. 5A**, the positively charged VP3 Ct shows the highest affinity for the membrane due to the deprotonation of the acidic lipids at pH 8, resulting in a net negative charge on the membrane surface (*SI Appendix*, Fig. S6). However, the electroneutral construct VP3 ΔNt has a lower binding energy than VP3 Ct, and also VP3 FL shows some degree of membrane

binding, despite both the protein and the membrane being negatively charged, as evidenced by the shallow minimum in the PMF.

The binding of the three protein constructs is strongly affected by electrostatics, as shown in **Fig. 5D**, where the adsorption energy is plotted as a function of the concentration of salt. The effect of salt concentration is most significant for VP3 Ct, but it is also noticeable for VP3 ΔNt and VP3 FL. Also, the interfacial concentration of each construct is higher at lower ionic strengths, as depicted in *SI Appendix*, Fig. S7. The weak binding energy of VP3 FL to the anionic membrane under physiological conditions (~150 mM NaCl, pH 7) is consistent with the experimental observation that VP3 FL does not bind to liposomes PA and PI, which are anionic at the pH of the experiments. However, those same experiments showed that VP3 FL did bind to PI3P(+) liposomes (**Fig. 1B-C**), despite the MT calculations predicting weak binding. Taken together, our results suggest that specific VP3-PI3P interactions enhance the binding of VP3 to PI3P-containing EE membranes, while exhibiting weak and non-specific electrostatic attractions to an otherwise generic anionic membrane. *SI Appendix*, Fig. S8 illustrates the distribution of charged residues of VP3 near the membrane, indicating that the Ct fragment drives the non-specific binding (*SI Appendix*, Fig. S9).

Molecular Dynamics (MD) simulations based on the MARTINI model were employed to investigate the mechanism by which VP3 Ct and VP3 ΔNt approach the membrane surface. We chose VP3 ΔNt over VP3 FL because VP3 ΔNt has a closer resemblance to the well-established experimental crystal structure. Additionally, the adsorption free energy profiles predicted by MT for both VP3 ΔNt and VP3 FL are notably similar (compare panels B and C of Figure 5). Unlike the MT model, MARTINI considers both electrostatic and van der Waals forces (De Jong et al., 2013). To mimic the liposome PI3P(+) composition used in the co-flotation assays, the lipid bilayer was modeled with a molar ratio of 64:31:5 for the lipids DOPE, DOPC, and PI3P, respectively. DOPE and DOPC are electroneutral, PI3P is anionic. The MD

simulations revealed that both VP3 Ct and VP3 ΔNt settled on the membrane surface after 120 ns, as shown in *SI Appendix,* Fig. S10A. **Figure 6A-D** shows a temporal sequence of configurations during the adsorption of VP3 ΔNt. The protein approached the membrane via the Ct fragment and remained adsorbed during the rest of the 500 ns trajectory. VP3 Ct exhibited the same behavior, as demonstrated in *SI Appendix*, Fig. S10A and Fig. S11. Notably, VP3 Ct and VP3 ΔNt did not detach from the surface during these MD simulations, suggesting that the adsorption energies calculated by MT were underestimated. Also, **Fig. 6E** highlights the location of the four positive residues that make up the P2 region, showing their proximity to the membrane surface.

**Recruitment of PI3P modulates the membrane binding of VP3.** We investigated the impact of VP3 Ct and VP3 ΔNt on the composition of the membrane near the binding point, and on the local curvature of PI3P(+) liposomes. We resorted to our MD simulations and evaluated the in-plane radial distribution function, g(r), between the center of mass of the proteins and the center of mass of PI3P molecules in the (cis) hemilayer, which is in direct contact with the protein. **Figure 6F** shows that VP3 Ct recruits PI3P within a ~2 nm radius, where its local concentration in the cis hemilayer is up to 6 times greater than the average PI3P concentration. Also, despite having no net electrical charge, VP3 ΔNt induces a similar concentration enhancement, with PI3P accumulation occurring around the Ct fragment, as evidenced in *SI Appendix,* Fig. S12. In both cases, the recruitment of PI3P in the cis hemilayer is accompanied by a local depletion of PI3P in the trans hemilayer, due to interhemilayer electrostatic repulsions (*SI Appendix,* Fig. S12). The effects on PI3P concentration, induced by VP3 ΔNt, result from a synergistic action between the positively charged Ct and the P2 region of the protein. Furthermore, when mutations are introduced to the P2 region - starting with $R_{200}D$ and eventually including the entire P2 domain - there is a gradual reduction in its contribution to the recruitment of PI3P (see *SI Appendix,* Fig. S14). Finally, to

examine the potential impact of VP3 on the lipid bilayer, we incubated liposomes PI3P(-) and PI3P(+) with purified His-VP3 FL as described previously. The samples were cryo-fixed and cryo-EM was used to observe the resulting structures. As shown in **Fig. 6G**, His-VP3 FL distorts the membrane of liposomes containing PI3P, resulting in small pinches in the bilayer, detectable in 36% of the liposomes PI3P(+), while it is completely absent in PI3P(-) liposomes. Taken together, our findings suggest that the binding of VP3 to EE membranes has the potential to alter the local lipid composition by recruiting PI3P, which could then lead to the localized membrane pinches observed in **Figure 6G**.

## Discussion

Several viruses hijack the PI3P metabolism machinery to complete their infectious cycle. However, only a few cases of viral proteins that bind PI3P have been described. Equine infectious anemia virus (EIAV) is a member of the lentivirus subgroup of retroviruses and replicates in macrophages. Retroviral assembly and release are directed by the structural precursor polyprotein Gag (Wills and Craven, 1991). EIAV Gag localizes to both the cell interior and to the plasma membrane due to its high-affinity interaction with PI3P (Fernandes et al., 2011; Puffer et al., 1998; Tanzi et al., 2003). Moreover, mutation of $K_{49}$, a residue in the PIs-binding pocket of Gag inhibited the release of viral-like particles from the plasma membrane (Fernandes et al., 2011). Another example are the poxviruses, a family of cytoplasmic DNA viruses that also rely on intracellular membranes to develop their envelope, whose morphogenesis requires enzymes from the cellular phosphoinositide metabolic pathway (Mcnulty et al., 2010). For vaccinia virus (VACV), the prototypic poxvirus, Kolli and coworkers showed that the VACV H7 protein binds to PI3P and PI4P (Kolli et al., 2015). Similarly to our observations in IBDV VP3, the authors uncovered two regions of

H7 essential for viral replication. One region is a positive surface patch centered on $K_{108}$, and the other region is the flexible Ct tail (Kolli et al., 2015).

Our biophysical and molecular simulation results suggest a specific but weak interaction of VP3 with PI3P bearing membranes. In co-floatation assays, we observed that His-VP3 FL reaches the top of the gradient, where liposomes PI3P(+) are located, with a high proportion of protein still found at the bottom of the gradient. This phenomenon was not observed with the His-2xFYVE protein. Additionally, the slopes of the BLI curves show that His-VP3 FL dissociate faster than His-2xFYVE from liposomes PI3P(+). Computer simulations have also revealed a weak attractive interaction between the negatively charged VP3 and membranes that contain PI3P. VP3 bears multiple essential roles during the viral life cycle. In this context, our hypothesis is that an early, specific, but weak interaction with PI3P is required for the formation of RCs associated with EE and represents an advantage for the virus that counts with VP3 to go forward into the replication cycle.

It has recently been reported that the RCs of IBDV exhibit liquid-liquid phase separation (LLPS) (Reddy et al., 2022). In LLPS, one or more biomolecules form a network of mild homo- and heterotypic interactions, resulting in the formation of a distinct liquid phase within a liquid medium (Banani et al., 2017). In light of our results, it is conceivable to hypothesize that viral interaction with the EE membranes acts as a first step in the RCs biogenesis, leading to the growth of biomolecular condensates with LLPS characteristics around EE membranes, as recently proposed (Brodrick and Broadbent, 2023). In support of this model, both the RNA dependent RNA polymerase VP1 and the viral dsRNA associate to endosomes (6) and to the LLPS condensates (Delgui et al., 2013; Reddy et al., 2022). Further experiments are needed in order to link the association of VP3 to EE membranes with biomolecular condensate formation.

## Evolutionary links between +sRNA and dsRNA viruses

Birnaviruses integrate the double-strand RNA Baltimore group (Baltimore, 1971), and the newly created *Riboviria* taxon (a realm), that includes all RNA viruses encoding RpRds. (Walker et al., 2021).These viruses contain highly divergent RpRds, all of which contain the "palm domain" comprising A-B-C sequence motifs crucial for catalysis (Wolf et al., 2018). However, birnaviruses, as well as RpRds from *Thosea asigna* virus (TaV) and the closely related Euprosterna elaeasa virus (EeV), two insect-specific +sRNA viruses belonging to the *Permutotetraviridae* family, include RdRps with a unique C-A-B motif arrangement in the palm subdomain (Gorbalenya et al., 2002). The membrane association of their replication complexes is a further specificity of birnaviruses that links them more to the +sRNA viruses than to the other dsRNA viruses. The crystal structure of the IBDV particle showing that birnaviruses possess a single icosahedral capsid T = 13 had already indicated strong links between birnaviruses and +sRNA viruses, placing them in a special branch of the dsRNA viruses that appears to have evolved independently of the others (Coulibaly et al., 2005). Indeed, within the megataxonomy merging together Baltimores´ and Linnean classification proposed by Koonin *et al*., the *Birnaviridae* family status is uncertain (Koonin et al., 2020).

## Materials and Methods

**Liposome preparation.** Liposomes were freshly prepared by the freeze-thaw and extrusion method (F Olson, C A Hunt and W J Vail, 1979). Briefly, lipids dissolved in chloroform were mixed and placed in glass vials, and the chloroform was evaporated by centrifuging 2 h at 35ºC in a SpeedVac. The dried lipids were resuspended in a binding buffer composed of 150 mM NaCl, 20 mM Tris-HCl, pH 8 to a final concentration of 5 mM. The preparation was submitted to ten cycles of freezing in liquid nitrogen

and thawing in a 37°C water bath. To generate small unilamellar liposomes, the multilamellar lipids were extruded through polycarbonate membranes (pore size 200 nm, Whatman). The liposomes were used within 1 week. The lipids POPE (1-palmitoyl-2-oleoyl-sn-glycero-3-phosphoethanolamine), POPC (1-palmitoyl-2-oleoyl-sn-glycero-3-phosphocholine), PI3P [1,2-dioleoyl-sn-glycero-3-phospho-(1'-myo-inositol-3'-phosphate)], PA (1,2-dioleoyl-sn-glycero-3-phosphate) and PI [1,2-dioleoyl-sn-glycero-3-phospho-(1'-myo-inositol)] were purchased from Avanti Polar Lipids. Liposomes PI3P(-) liposomes were prepared as a mixture of POPE and POPC at a molar ratio of 64:36. Liposomes PI3P(+), PA(+) or PI(+) were prepared as a mixture of POPE and POPC, with either PI3P, PA or PI at a molar ratio of 64:31:5.

**Liposome co-flotation assay**. For liposome co-flotation assays, the following proteins were used: the IBDV VP3 full length (FL) protein [strain Soroa, GenBank AF140705.1, residues 756-1012 (257 residues) from the polyprotein], a Ct truncated version of VP3, VP3 Δ223-257, a point mutant where the arginine (R) 200 was replaced by an aspartic acid (D), VP3 FL $R_{200}D$ and 2xFYVE Hrs domain [*Mus musculus*, GenBank D50050.1, residues 147-223 (77 residues)] (Komada and Kitamura, 1995). They were produced with a histidine-tag in the Bac-to-Bac™ Baculovirus Expression System (Invitrogen, for VP3 proteins) or *Escherichia coli* prokaryotic system (for 2xFYVE). Then, 3 mM liposomes were incubated with 1 μM protein in binding buffer composed of 150 mM NaCl, 20 mM Tris-HCl, pH 8 at 4ºC overnight (on), in a final volume of 100 μl. Liposomes and liposome-protein complexes were separated from unbound protein by ultracentrifugation of the reaction mixture in 5 mL Optiprep™ (Axis-Shield PoC AS) density gradients for 1 hour at 40,000 ×g (SW55Ti Beckman Coulter rotor). The liposome-protein mixture was adjusted to 34% Optiprep concentration in a volume of 300 μl, and loaded onto the bottom of the tube that contained 4.5 ml of 20% Optiprep in 150 mM NaCl, 20 mM Tris-HCl,

pH 8, overlaid with 200 µl of the buffer. The three top and the bottom fractions, containing 400 µl of the gradient were used for SDS-PAGE gel analysis and immunoblotting against His-tag and anti-VP3 rabbit polyclonal serum.

**Recombinant prokaryotic-expression plasmids.** Plasmid encoding EGFP-2xFYVE, pEGFP-2xFYVE, was generated by Gillooly and collaborators (Gillooly et al., 2000) and kindly provided by Harald A. Stenmark (Norwegian Radium Hospital, Oslo, Norway) to our group. The 2xFYVE fingers used for this plasmid consisted in duplicated domains of residues 147-223 of mouse hepatocyte growth factor-regulated tyrosine kinase substrate (Hrs) (Komada and Kitamura, 1995) separated by a QGQGS linker. The prokaryotic vector expressing 2xFYVE was obtained following standard PCR methods with the oligonucleotide pair 2xFYVE (*SI Appendix*, Table 1). The PCR fragment was inserted into the pET32a(+), which incorporates the thioredoxin A (TrxA) gene, a 6xHis tag and Thrombin site (Ts) within the amino-terminal domain of the 2xFYVE, and the correctness of the insertion was confirmed by sequencing. The complete fusion protein TrxA.His.Ts.2xFYVE is 954 base pairs (bp)-long and contains 317 residues (~35 kDa). Plasmids pET32a(+) encoding VP3 FL and Δ223-257 were obtained by subcloning the corresponding DNA fragments which were previously amplified from pcDNAVP3 FL using standard PCR methods with the oligonucleotide pairs VP3.FL and VP3. Δ223-257, respectively (*SI Appendix*, Table 1). The complete fusion proteins contain: VP3 FL 1167 bp (388 residues, ~43 kDa) and VP3 Δ223-257 1058 bp (352 residues, ~38 kDa).

**Recombinant baculoviruses.** The construct of the recombinant baculovirus (rBV) His-VP3 FL was generated from IBDV VP3 FL protein [strain Soroa, GenBank AF140705.1, residues 756-1012 (257 residues) from the polyprotein] cloned in pcDNA vector. Thus, IBDV VP3 FL protein was subcloned

from plasmid pcDNAVP3 FL into the pFastBacHTb vector (Gibco BRL), which incorporates a 6xHis tag at the N-terminal of the recombinant protein. Briefly, VP3 FL coding sequence was amplified by PCR with the oligonucleotide pairs VP3.Fw and VP3.Rv incorporating *Bam*HI and *Eco*RI restriction sites, respectively (*SI Appendix*, Table 1). The resulting DNA fragment containing the VP3 gene was digested with *Bam*HI and *Eco*RI and ligated to plasmid pFastBacHTb restricted with the same enzymes, generating the plasmid pFastBac-his-VP3 FL. This plasmid contained the VP3 gene fused to a histidine tag under the control of the polyhedrin promoter. The generation of rBV His-VP3 FL $R_{200}D$ was performed following the same procedure, but using the pcDNAVP3 FL $R_{200}D$ as a template for subcloning. The generation of rBV His-VP3 Δ223-257 was performed as follows. A 663 nucleotide DNA fragment containing a truncated version of the VP3 sequence encoding a polypeptide lacking the 36 carboxi-terminal residues was amplified by PCR from pcDNAVP3 FL with the oligonucleotide pairs VP3.Fw and VP3 Δ223-257.Rv incorporating *Bam*HI and *Eco*RI restriction sites, respectively (*SI Appendix*, Table 1). The DNA fragment was digested with *Bam*HI and *Eco*RI and was ligated to plasmid pFastBac HTb restricted with the same enzymes, generating the plasmid pFastBac-his-VP3 Δ223-257. All the resulting plasmids were subjected to nucleotide sequencing to assess the correctness of the inserted VP3 sequence, and they were then used to produce the corresponding rBVs by using the Bac-to-Bac system and by following the manufacturer's instructions (Invitrogen). Briefly, the recombinant plasmids were transformed into DH10Bac competent cells to obtain recombinant bacmids. The white colonies on culture plates were picked, confirmed by PCR and used for Sf9 cell transfection by using Cellfectin II Reagent (Gibco). The transfected cells were cultured at 28°C for 5 days to produce rBVs. Then, the cells were subjected to Western blot analysis for recombinant proteins expression confirmation and the supernatant (P1) was used to amplify the rBVs to a higher-titre P2 and scaled up to obtain a

higher volume of P3 to be titrated (Plate-Forme Technologique Production et Purification de Protéines Recombinantes, Institut Pasteur) and used for protein production.

**Protein expression and purification.** For the liposome co-flotation assays, His-VP3 polypeptides were produced with a histidine-tag in the Bac-to-Bac™ Baculovirus Expression System. Briefly, Sf9 cells (Gibco, ThermoFisher Scientific) were infected with recombinant Baculoviruses (rBVs) at a multiplicity of infection (MOI) of 5 PFU/cell. Cells were harvested at 96 h post-infection, washed once with chilled phosphate-buffered saline (PBS), resuspended in lysis buffer [50 mM Tris-HCl (pH 8.0), 500 mM NaCl, 0.1% nonidet P-40) supplemented with protease inhibitors (Complete Mini, Roche), and maintained on ice for 30 min. Thereafter, extracts were sonicated and centrifuged at 13.000 g for 15 min at 4ºC. Supernatants were collected and subjected to immobilized metal-affinity chromatography (IMAC) purification by using a $Ni^{2+}$ affinity column (HiTrap Fast Flow Crude, GE Healthcare). Resin-bound proteins were eluted with elution buffer [50 mM Tris-HCl (pH 8.0), 500 mM NaCl, 500 mM imidazole]. His-tagged VP3 FL, VP3 Δ223-257 or VP3 FL $R_{200}D$ -containing fractions were pooled and subjected to size exclusion chromatography using a Superdex 200 column (GE HealthCare). Finally, protein samples were concentrated to a final concentration of ~3 mg/ml by using Centricon filters (Millipore), aliquoted and flash-frozen in liquid nitrogen for -80ºC storage. For His-2xFYVE polypeptide, *E. coli* BL21 DE3 cells containing the plasmid pET32a(+)-2xFYVE were grown at 37°C until an OD 600 of 0.6 was reached. Protein expression was induced overnight at 18°C using 1mM IPTG. Cells were harvested via centrifugation, resuspended in buffer [10 mM TRIS-HCl (pH 8.0), 100 mM NaCl] supplemented with protease inhibitors and sonicated. The cell lysate was clarified via centrifugation at 18.000 g for 20 min at 4°C and the resulting supernatant was subjected to IMAC purification by using a $Ni^{2+}$ affinity column (HiTrap Fast Flow Crude, GE Healthcare). Resin-bound proteins were eluted with elution buffer [10 mM

TRIS-HCl (pH 8.0), 100 mM NaCl, 500 mM imidazole]. His-2xFYVE-containing fractions were pooled and subjected to size exclusion chromatography using a Superdex 75 column (GE HealthCare). Finally, protein samples were concentrated to a final concentration of ~3 mg/ml by using Centricon filters (Millipore), aliquoted and flash-frozen in liquid nitrogen for -80ºC storage. For BLI and cryo-EM experiments, His-VP3 polypeptides were purified following the same procedure as for His-2xFYVE. Purified 2xFYVE-GST peptides were produced by a classical GST fusion protein purification protocol, using pGEX-5X-1 vector (GE Healthcare, 27-4584-01) cloning as described (Nascimbeni et al., 2017). Briefly, *E. coli* BL21 DE3 strain maxi-cultures were lysed and subjected to glutathione beads binding for GST purification. The glutathione beads were finally treated with benzamidine-coated beads (GE Healthcare Life Science, 17512301) to remove the factor Xa and dialyzed for the final purification in a 75 mM KAc, 30 mM HEPES, pH 7.4, 5 mM $MgCl_2$ solution.

**Purified proteins quantification and quality control assessment.** His-tagged VP3 FL, VP3 Δ223-257, VP3 FL $R_{200}D$, and 2xFYVE quantification at 280 nm was carried out by recording a full spectrum between 240 and 340 nm. Measurements were done with 60 µL of buffer and sample at 20°C in a 1 cm quartz cell, reference 105.202-QS.10 (Hellma Analytics, France), using a JASCO V-750 spectrophotometer (JASCO Corporation, Japan). A baseline subtraction at 340 nm was performed with the Spectragryph software to accurately calculate the protein concentration. The assessment of the sample homogeneity was performed by Dynamic Light Scattering (DLS) analysis on a DynaPro Plate Reader III (Wyatt, Santa Barbara, CA, USA) to ensure that the samples did not contain aggregates. A volume of 20 µL of sample was loaded in a 384-well microplate (Corning ref 3540, New-York, USA), with 10 acquisitions of 5 s each at 20°C, monitored with the DYNAMICS version V7.10.0.21 software (Wyatt, Santa Barbara, CA, USA), three repetitions per measurement. Finally, the protein integrity and purity

were assessed by intact mass spectrometry on a Bruker UltrafeXtreme MALDI-TOF/TOF instrument. A volume of 15 µL of protein was passed through a ZipTip C4 and eluted on a MTP 384 ground steel target plate (Bruker-Daltonics, Germany) with 2 µl of a 20 mg/ml α-Cyano-4-hydroxycinnamic acid (HCCA) in 50% acetonitrile (ACN), 0.1% trifluoroacetic acid (TFA) as matrix solution. Data were acquired using Flexcontrol software (Bruker-Daltonics, Germany) and shots were recorded in positive ion linear mode. Mass spectra were externally calibrated in the m/z range of 15-60 kDa with the Protein II (Bruker-Daltonics, Germany) and analyzed with the Flexanalysis software (Bruker).

**Recombinant mammalian expression plasmids.** Plasmids encoding EGFP, EGFP-Rab5 and EGFP-Rab5 Q79L were kindly provided by Philip D. Stahl (Washington University, St. Louis, MO). Plasmids encoding GFP-2FYVE were kindly provided by Harald A. Stenmark (Norwegian Radium Hospital, Oslo, Norway). Plasmids pcDNAVP3 FL and pcDNAVP3 Patch 2 (P2 all reversed) were constructed by Valli and collaborators in a previous study (Valli et al., 2012) and kindly provided by José F. Rodríguez (CSIC, Madrid, Spain) to our group. The plasmids encoding point mutant VP3 proteins ($K_{157}D$, $R_{159}D$, $H_{198}D$ and $R_{200}D$) were obtained by site-directed mutagenesis. For this purpose, the plasmid pcDNAVP3 FL was used as template DNA in polymerase chain reactions (PCR) together with oligonucleotide primer pairs containing changed nucleotides in order to generate the point mutations (*SI Appendix*, Table 1). PCRs were carried out using Pfu DNA polymerase (PB-L, Argentina) and the following conditions: initial DNA denaturation at 95ºC for 5 min followed by 30 cycles of 95ºC for 1 min, 65ºC for 1 min and 72ºC for 6 min and a final extension at 72ºC for 10 min. The size of the amplified products was corroborated by agarose gel electrophoresis. In order to degrade the plasmid mold, the PCR mixtures were incubated with *Dpn*I endonuclease (ThermoFisher Scientific, USA) at 37ºC for 2 h followed by heating at 80ºC for 20 min. Aliquots of those reactions were transformed into competent *E. coli* DH10B

cells (Invitrogen, USA). Colonies carrying the mutated plasmids were selected in LB plates containing ampicillin (100 µg/mL). Plasmids were purified using the EasyPure® Plasmid MiniPrep Kit (TransGen Biotech Co., Ltd, China) and the introduction of mutations was confirmed by nucleotide sequencing (Macrogen service, South Korea). Alignments and prediction of amino acid sequences were performed using the Aligner and Translator tools from the JustBio website ("JustBio," n.d.).

**Cryo-electron microscopy.** Protein-liposome complexes prepared as described above. Briefly, 3 mM liposomes composed of POPE, POPC and PI3P (molar ratio of 64:31:5) or composed of POPE and POPC (molar ratio of 64:36) were incubated with 1 mM protein in a binding buffer composed of 150 mM NaCl, 20 mM Tris-HCl, pH 8 in the final volume of 100 µl. After overnight incubation at 4ºC, 4 µl of the samples were spotted on glow-discharged lacey grids (S166-3, EMS) and cryo-fixed by plunge freezing at -180°C in liquid ethane using a Leica EMGP (Leica, Austria). Grids were observed with a Tecnai F20 electron microscope (Thermo Fisher Scientific). The Tecnai F20 was operated at 200 kV and images were acquired under low-dose conditions using the software EPU (Thermo Fisher Scientific) and a direct detector Falcon II (Thermo Fisher Scientific). For immunogold staining, 1.5 µL of purified His-protein 0.3 mM were first incubated with 5 µL of Ni-NTA [nickel (II) nitrilotriacetic acid] gold particles 0.5 mM (five times gold particles/purified protein) in binding buffer to a final volume of 10 µl. This reagent comprises 5 nm gold particles covered with multiple Ni-NTA functionalities incorporated into the ligands on the surface of gold particles. Each $Ni^{2+}$ coordinates with one NTA and two histidines from the His-tagged recombinant protein to form a stable complex with extremely low dissociation constants (Reddy et al., 2005). Then, 4 µl of this mix were incubated with 6 µl of 3 mM liposome preparation on at 4ºC. Finally, 4 µl of each complex was subjected to cry-fixation and cryo-EM analyzed as mentioned.

**Transient transfections and indirect immunofluorescence assay.** QM7 cells were grown on coverslips in an M24 multi-well plate for 12 h to approximately 70% confluence and then plasmids were transfected employing Lipofectamine 3000 (number L300015; Thermo Fisher, Argentina) following the manufacturer's recommendations. After 24 h p.i., the cells were fixed with 4% paraformaldehyde (PFA) for 15 min at room temperature (RT), washed with PBS (pH 7.4), and permeabilized with 0.05% saponin in PBS containing 0.2% bovine sero albumin (BSA) for 20 min at RT. Then the cells were incubated with anti-VP3 primary antibodies overnight (ON) at 4ºC in a humidity chamber, and after extensive washing, cells were incubated with secondary antibodies conjugated with Alexa Fluor Cy3 for 1 h 30 min, followed by extensive washes in PBS. The coverslips were mounted in Mowiol plus Hoechst and analyzed by Confocal Laser Scanning Microscopy (CLSM). Images were captured using an Olympus FluoView TM FV1000 confocal microscope (Olympus, Argentina) with FV10-ASW (version 01.07.00.16) software and processed using the ImageJ software (Schindelin et al., 2012). For quantification of VP3 cellular distribution (Fig. 2D), the percentage of cells with vesicular distribution of the red signal was calculated out of approximately 30 cells per construct and experiment. For quantification of the co-localization of VP3 and either EGFP-Rab5 orEGFP-2xFYVE, the Manders $M_2$ coefficient was calculated out of approximately 30 cells per construct and experiment (*SI Appendix*, Fig. S3 and Fig. 3A, respectively). The M2 coefficient, which reflects co-localization of signals, is defined as the ratio of the total intensities of red image pixels for which the intensity in the green channel is above zero to the total intensity in the red channel. JACoP plugin was utilized to determine M2 (Bolte and Cordelières, 2006). For VP3 puncta co-distributing with EEA1 and GST-FYVE the number of puncta co-distributing for the three signals were manually determined out of approximately 40 cells per construct and experiment per 200 $\mu m^2$ (**Fig. 3B**).

**Reverse genetics.** For the generation of recombinant IBDV we used a modification of the reverse genetics system described by Qi and coworkers (Qi et al., 2007), in which the full-length sequences of the IBDV segments, flanked by a hammerhead ribozyme at the 5'-end and a hepatitis delta ribozyme at the 3'-end, are expressed under the control of an RNA polymerase II promoter. For its construction, the complete segments of IBDV Soroa were amplified from viral dsRNA using a sequence independent amplification method (Potgieter et al., 2009) and cloned in plasmid pJET1.2 (Thermo Fisher Scientific). The hammerhead ribozymes, specific for each segment, are based in the HamRz-R, described by Yanay and cols. (Yanai et al., 2006), with 10 nucleotides of sequence complementary to each IBDV segment stabilizing Stem I. At the 3'-end, we used the sequence of the antigenomic hepatitis delta ribozyme HDVagrz SC (Ghanem et al., 2011). DNA fragments containing the ribozyme sequences were constructed by PCR-based gene synthesis with oligonucleotides designed by the Assembly PCR Oligo Maker software (Rydzanicz et al., 2005). Each PCR-amplified IBDV full-length segment were cloned, flanked by the corresponding hammerhead ribozyme and HDVagrz SC, between the *Eco*RI and *Not*I sites of plasmid pCAGEN [a gift from Connie Cepko; Addgene plasmid # 11160; (Matsuda and Cepko, 2004a)] by Gibson assembly (Gibson et al., 2009). The correctness of the sequences in both plasmids, pCAGEN.Hmz.SegA.Hdz (SegA) and pCAGEN.Hmz.SegB.Hdz (SegB), was assessed by sequencing (Eurofins Scientific). The plasmid pCAGEN.Hmz.SegA.$R_{200}$D.Hdz (SegA.$R_{200}$D) was purchased to GenScript and the mutation was verified by sequencing of the complete plasmid (Eurofins Scientific).

**Recombinant viruses foci forming units assay.** QM7 cells were grown in M24 multi-well plates for 12 h to approximately 90-95% confluency and then 800 ng (400 ng of plasmid with each segment) were transfected by using Lipofectamine 2000 (number 11668027; Thermo Fisher, Spain) following the

manufacturer's recommendations. When performing single segment transfections (SegA, SegB and SegA.$R_{200}$D), 400 ng of the plasmid pCAGIG (a gift from Connie Cepko; Addgene plasmid #11159; (Matsuda and Cepko, 2004b)) was added to 400 ng of those containing the viral segments to reach a total of 800 ng of total DNA per transfection. pCAGIG is a mammalian expression vector that shares the backbone with the pCAGEN vector used for the expression of the viral segments. The following transfections were performed in triplicate: SegA, SegB, SegA.$R_{200}$D, SegA+SegB or SegA.$R_{200}$D+ SegB. At 8 h post-transfection (p.t.) the supernatants were discarded and the monolayers were recovered for further plating on M6 multi-well plates containing non transfected QM7 cells. For monolayers transfected with SegA, SegB, SegA.$R_{200}$D and SegA.$R_{200}$D+ SegB half of the transfected monolayer was plated on fresh cells. For SegA+SegB, which leads to the production of wild type virus, several dilutions were tested, always in triplicate. To limit virus diffusion and facilitating the foci forming Avicel RC-591 (FMC Biopolymer) was added to the M6 multi-well plates. 72 h p.i., the monolayers were 16% formaldehyde-fixated and stained with Coomassie R250 (BioRad).

**Statistical analysis.** One-way ANOVA followed by a Tukey's HSD (honestly significant difference) test were performed using AnalystSoft Inc., StatPlus:mac - Version v8 ("AnalystSoft Inc., StatPlus:mac - v8," n.d.). Plotting was done using the *ggplot2* package (Wickham, 2016) in R, with assistance from the RStudio software (RStudio Team, 2020).

**Bioinformatics analysis.** Multiple sequence alignment and the percent identity matrix were performed with Clustal OMEGA (v1.2.4) (Sievers et al., 2011) implemented at EMBL's European Bioinformatics Institute ("EMBL's European Bioinformatics Institute," n.d.). Accession numbers of the sequences: Infectious bursal disease virus (AF_140705.1); Blotched snakehead virus (YP_052872.1); Victorian

trout aquabirnavirus (YP_009255397.1); Tellina virus 2 (YP_010084301.1); Yellowtail ascites virus (NP_690805.1); Infectious pancreatic necrosis virus (NP_047196.1); Tasmanian aquabirnavirus (YP_009177608.1); Lates calcarifer birnavirus (YP_010086267.1) and Tellina virus 1 (YP_009509080.1). Alignment visualization was done with the R *ggmsa* package (Zhou et al., 2022) with the assistance from the RStudio software (RStudio Team, 2020). Amino acids are colored according to their side-chain chemistry. Protein sequence logos annotation is displayed on top of the amino acid alignment.

The model of VP3 FL from IBDV ([strain Soroa, GenBank AF140705.1, residues 756-1012 (257 residues) from the polyprotein] was generated using a local copy of AlphaFold-2 (Jumper et al., 2021), installed using the open-source code available at https://github.com/deepmind/alphafold (accessed on 1 September 2021). Runs were performed on a Centos 7 workstation with 64 CPUs and 4 GeForce RTX 2080 Ti GPUs, using the casp14 preset and including all PDB templates present in the database. The program produces a per-residue confidence metric termed pLDTT on a scale from 0 to 100. pLDTT values higher than 70 reflect reliable models with correct backbone predictions, and those with values higher than 90 correspond to models with both reliable backbone and side-chain orientation predictions. pLDTT values lower than 50 are a strong predictor of disorder, and regions with such values are either unstructured under physiological conditions or only structured as part of a complex.

**Reagents and antibodies.** Western blot and confocal laser scanning microscopy (CLSM) analyses were carried out using rabbit anti-VP3 specific sera followed by horseradish peroxidase (HRP)-conjugated anti-rabbit secondary antibodies (number A0545), purchased from Sigma-Aldrich (Buenos Aires, Argentina). For early endosomes detection by CLSM, we used anti-EEA1 mouse monoclonal antibody (1:200 dilution; BD Transduction Laboratories, 610456), and for anti-GST detection, we used Alexa

Fluor 649-labelled goat anti-GST (Rockland-Inc, 600-143-200). Fluorescently labelled secondary antibodies, all diluted 1:200 from Invitrogen, included Alexa Fluor 546 donkey anti-mouse (A10036), and Alexa Fluor 546 donkey anti-rabbit (A10040).

**Far-UV circular dichroism (CD) of VP3 proteins.** Soluble VP3 FL and VP3 FL $R_{200}D$ at a concentration of 2 mg/ml in 50 mM Tris-HCl pH 8, 500 mM NaCl were analysed by far-UV CD (180-260 nm). CD spectra were obtained with an AVIV CD spectropolarimeter model 215 using a 0.02 cm path length cell at RT. Five successive scans were averaged and the background spectrum of the sample buffer, acquired under identical conditions, was subtracted. The resulting corrected CD intensities were then converted to $\Delta\varepsilon$ per residue. Secondary structure contents were estimated from the far-UV CD spectra using the CDSSTR routine (Johnson, 1999) of the DICHROWEB server (Whitmore and Wallace, 2008, 2004) run on the SP175 reference dataset (Lees et al., 2006), containing 72 proteins representing a large panel of secondary structures. Similar results were obtained on different datasets (Sreerama and Woody, 2000) or by using the CONTIN/LL routine (Provencher and Glöckner, 1981).

**Coarse Grain (CG) models of VP3 constructs.** Three protein constructs derived from VP3 were considered: 1. VP3 Ct. A peptide comprising the last 36 residues of VP3 (223 to 257) ending in the Ct. VP3 Ct has an overall electrical charge of +5, and is absent from the available crystal structure of VP3. Consequently, it was assumed to be a disordered domain and was modeled as unstructured. 2. VP3 Δ81. A shorter version of VP3 that lacks the first 81 residues leading to the Nt. It consists of the crystallized structure of the protein core (residues 82 to 222, available from the Protein Data Bank PDB ID 2R18), concatenated with the VP3 Ct peptide. As the first 9 residues of the protein core are also missing from resolved structure, they were modeled as unstructured, similar to the VP3 Ct fragment. VP3 Δ81 was

selected primarily because it contains the structural information of the crystallized protein, which provides valuable insights into the protein's overall structure and function. In addition, the construct includes the Ct peptide (VP3 Ct), which is crucial for membrane binding. Although the Nt 81 residues are absent in this construct, their exclusion was found to be inconsequential in terms of evaluating the protein's binding energy and positioning on the membrane surface (compare, for example, VP3 Δ81 and VP3 FL in Figure 5). 3. VP3 FL. The full-length VP3 protein, which was obtained as an AlphaFold prediction (Jumper et al., 2021). The structure of the protein predicted by AlphaFold not only provided insight into the overall architecture of VP3, but it also reinforced our model of unstructured VP3 Ct. It is worth noting that the Nt 81 residues, which are absent in VP3 Δ81, are predicted to be in a modular conformation, constituting a globular domain separated by a loop from the globular domain of the core region (crystallized residues 82 to 222). The structural information provided by the full-length VP3 model is therefore useful in understanding the interaction with lipid membranes.

All proteins were modeled with the MARTINI force-field (De Jong et al., 2013) [whenever needed, the secondary structure of the non-disordered protein domains was restrained by means of the ElNeDyn elastic network model (elnedyn22)] (Periole et al., 2009; Poma et al., 2017). In this case, harmonic potentials with a force constant of 1000 kJ $mol^{-1}$ $nm^2$ were applied between backbone particles separated by less than 1.4 nm. In the construction of VP3 Δ81, elastic network restrictions were applied to residues 91 to 220, which was the fragment resolved from by crystallography. However, in VP3 FL, the elastic network was applied to all globular domains, while leaving the linkers and the last 36 residues at the Ct unrestricted.

**Molecular Theory calculations.** The Molecular Theory (MT) used to assess protein adsorption is detailed in references (Chiarpotti et al., 2021; Ramírez et al., 2019). Briefly, this mean-field method

yields the distribution of macromolecules in an anisotropic system, through the minimization of a model free-energy functional that accounts for electrostatic and steric interactions, the configurational and translational entropy of the macromolecules, the translational entropy of the free species (protons, hydroxyls, and salt ions) and the acid-base equilibrium of all ionizable molecules in the system. In the present case, the membrane was modeled as a dielectric slab of thickness h, with a dielectric constant $\varepsilon_M$, which is in contact with a solution of dielectric constant $\varepsilon_S$. Far from the membrane ($z \rightarrow \infty$), the solution is in contact with an infinite bulk that contains the proteins (1 μM concentration), all the free species, and a fixed pH=8. The rigid membrane contained 15% of ionizable groups on its surface, in order to mimic the 5% of ternary ionizable PI3P. One third of these groups were assigned a $pK_a$ of 2.5, corresponding to the phosphate group of the glycerol moiety, while the $pK_a$ for the rest was set to 6.5, corresponding to the phosphoesther groups of inositol. MT requires the input of a large set of protein conformations, which are subsequently reweighted by the theory. These conformations were generated by Molecular Dynamics simulations of the proteins in water. VP3 Ct, VP3 Δ81 and VP3 FL were modeled using MARTINI-2.2 parameters (Marrink et al., 2007). The proteins were hydrated in MARTINI polarizable water. As stated before, the proteins globular segments (residues 92-222 in both VP3 Δ81 and VP3 FL, and residues 7-79 additionally in VP3 FL) were restricted through the application of the elastic network ElNeDyn (Marrink et al., 2007) with a spring constant of 1000 $kJ.mol^{-1}$ applied to backbone beads (BB) within a cutoff distance of 1.4 nm. Each protein was simulated for 100 ns, after equilibration, in the NPT ensemble using GROMACS 2021.3. A cluster analysis was performed in order to obtain the most representative conformations of the simulated ensemble. This method groups conformations by structural similarity, using the root mean squared deviation (RMSD) of the coordinates calculated for all conformer pairs along the trajectory, clustering structures with RMSD ≤ 0.3 nm. This procedure leads to 50 conformers

for each protein construct. Each conformer was subsequently rotated 30 times randomly to produce a set of 1500 configurations for the MT calculations.

**Molecular Dynamics Simulations of VP3 on a lipid bilayer.** MARTINI-2.2 was also used to model the lipid molecules in our MD simulations. The bilayer was assembled using insane utility (Wassenaar et al., 2015), while hydration with polarizable water molecules and ions was performed with the solvate utility of the GROMACS package. The bilayer had a symmetric lipid composition of 30% 1,2-dioleoyl-sn-glycero-3-phosphocholine (DOPC), 65% of 1,2-dioleoyl-sn-glycero-3-phosphoethanolamine (DOPE) and 5% 1,2-dioleoyl-sn-glycero-3-phosphatidylinositol-3-phosphate (PI3P), leading to a lipid composition of 111:231:18 (DOPC, DOPE, and PI3P) in each leaflet. The protein was placed at a distance of 10 nm from the membrane surface, to avoid a possible initial binding bias. The system was then equilibrated and finally simulated for 500 ns. Both equilibration and production were in the NPT ensemble. A semi-isotropic Parinello-Rahman barostat (Parrinello and Rahman, 1981) with a 12 ps time constant, and lateral and normal compressibilities of $3\times10^{-4}$ $bar^{-1}$ were used to keep the pressure at 1.0 bar. The v-rescale thermostat, with a time constant of 1 ps, was used to keep the temperature at 325 K. In all cases the integration timestep was 20 fs. Long range electrostatics were calculated using the particle mesh Ewald (PME) method (Darden et al., 1993) with a real-space cut-off of 1.2 nm.

## Acknowledgments

This project was partially supported by: the National Agency for Scientific and Technological Promotion, Ministry of Science, Technology and Innovation, through grants PICT 2016-0528 and 2019-01324 to L.R.D; PICT 2015-2210 to F.A.Z; PICT 2019-01889 to L.M.P. and PICT 2020-3795 to M.G.D.P; the

National Scientific and Technical Research Council through grants PIP 2015-2017 11220150100114CO and 2021-2023 11220200103139CO to L.R.D.; 2021-2023 11220200103195CO to L.M.P. and 11220200103223CO to M.G.D.P.; and by the National University of Cuyo through grants 2013-2015 M006, 2016-2018 M029, 2019-2021 M071 and 2022-2024 M012 to L.R.D. For stays performed by L.R.D. in the laboratory of Structural Virology at the Institut Pasteur in Paris, we are grateful for the support of National University of Cuyo through the Teaching Staff Mobility Program in 2018-2019, the Ministry of Education through the Program scholarships for training abroad in Science and Technology (**BEC**.AR 2018), and the International Union of Biochemistry and Molecular Biology (IUBMB) through a "2020 Mid-Career Research Fellowship". The work in Madrid was supported by grants from the Spanish Ministry of Science and Innovation (PID2020-113287RB-I00) and the Comunidad Autónoma de Madrid (P2018/NMT-4389) to JRC. At the IHEM, we sincerely appreciate Elisa Bocanegra, Norberto Domizio, and Jorge Ibañez for valuable technical assistance in CLSM handling. At the Institut Pasteur in Paris, we are grateful to Gérard Pehau-Arnaudet and the staff at the Ultrastructural BioImaging core facility for image acquisition and analysis; to Patrick England and Sébastien Brûlé and the staff of the Molecular Biophysics platform for purified protein analyses, CD and BLI assays, to Stéphane Petres and members at the Production and Purification of Recombinant Proteins Technological Platform, and to the staff of the Proteomics platform.

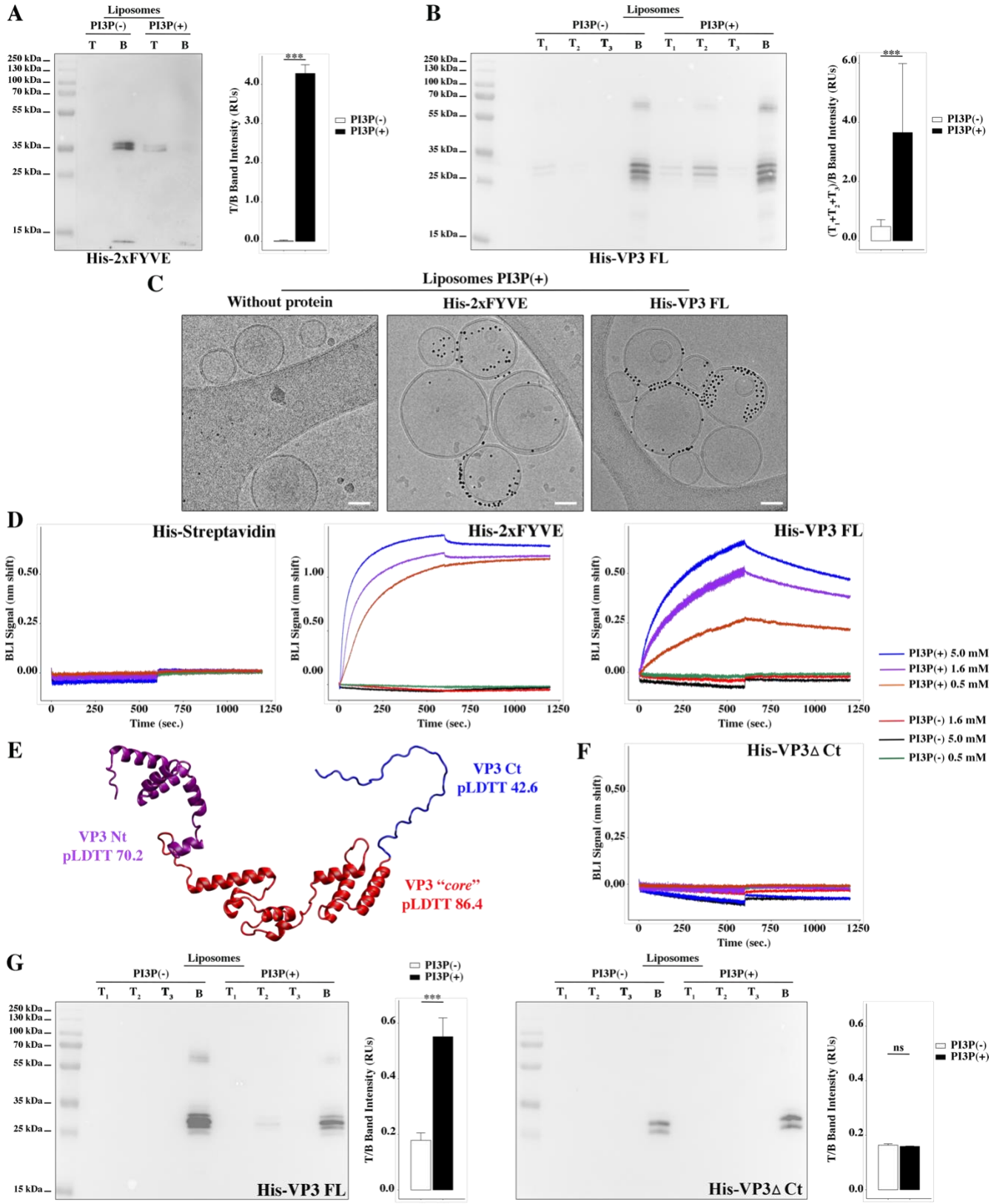
A
Liposomes
PI3P(-)
PI3P(+)
T B T B
250 kDa
130 kDa
100 kDa
70 kDa
55 kDa
35 kDa
25 kDa
15 kDa
His-2xFYVE
T/B Band Intensity (RUs)
***
PI3P(-)
PI3P(+)
B
Liposomes
PI3P(-)
PI3P(+)
T1 T2 T3 B T1 T2 T3 B
His-VP3 FL
(T1+T2+T3)/B Band Intensity (RUs)
C
Liposomes PI3P(+)
Without protein
His-2xFYVE
His-VP3 FL
D
His-Streptavidin
His-2xFYVE
His-VP3 FL
BLI Signal (nm shift)
Time (sec.)
PI3P(+) 5.0 mM
PI3P(+) 1.6 mM
PI3P(+) 0.5 mM
PI3P(-) 1.6 mM
PI3P(-) 5.0 mM
PI3P(-) 0.5 mM
E
VP3 Ct
pLDTT 42.6
VP3 Nt
pLDTT 70.2
VP3 "core"
pLDTT 86.4
F
His-VP3Δ Ct
BLI Signal (nm shift)
Time (sec.)
G
Liposomes
PI3P(-)
PI3P(+)
T1 T2 T3 B T1 T2 T3 B
His-VP3 FL
T/B Band Intensity (RUs)
***
His-VP3Δ Ct
ns

703

**Figure 1. Biophysical characterization of VP3 binding to PI3P.**

**(A)** Immunoblots of the top (T) and bottom (B) fractions from a liposome PI3P(-) or PI3P(+) OptiprepTM co-floatation assay indicating that His-2xFYVE protein specifically binds to liposome PI3P(+). Results are representative of three independent experiments. The bar plot represents the intensity of T/B bands for each liposome preparation. Significant differences (** $P$ <0.01) as determined by one-way ANOVA with Tukey's HSD test.

**(B)** Immunoblots of the three top ($T_1$, $T_2$ and $T_3$) and bottom (B) fractions from a liposome PI3P(-) or PI3P(+) OptiprepTM co-floatation assay indicating that His-VP3 FL protein specifically binds to liposome PI3P(+). Results are representative of three independent experiments. The bar plot represents the intensity of ($T_1$+$T_2$+$T_3$)/B bands for each liposome preparation. Significant differences (* $P$ <0.05) as determined by one-way ANOVA with Tukey's HSD test.

**(C)** Cryo-electron microscopy images of cryo-fixated liposomes PI3P(+) control (without protein), or incubated with His-2xFYVE- or His-VP3 FL-Ni-NTA gold particles showing gold particles decorating the membrane of the liposomes when His-2xFYVE or His-VP3 FL were present. The bar represents 50 nm.

**(D)** Binding of His-Streptavidin (negative control), His-2xFYVE (positive control) or His-VP3 FL to three different concentrations of liposomes PI3P(-) or PI3P(+). Association and dissociation sensorgrams measured by bio-layer interferometry (BLI), showing the specific interaction of His-2xFYVE and His-VP3 FL with liposomes PI3P(+) in a dose-dependent manner, as indicated.

**(E)** Cartoon representation of AlphaFold prediction of VP3 FL. Red region corresponds to the "*core*" region of the protein present in the experimental X-ray crystallographic model obtained by Casañas *et al*., 2008 [PDB: 2R18 (Casañas et al., 2008)]. Regions not present within the PDB are colored in violet

and blue representing the Nt and the Ct of VP3, respectively. pLDTT values lower than 50 are a strong predictor of disorder.

**(F)** Binding of His-VP3 ΔCt to three different concentrations of liposomes PI3P(-) or PI3P(+). Sensorgrams measured by BLI, showing the absence of binding to either liposomes when the VP3 lacks the Ct region [blue in (E)].

**(G)** Immunoblots of the three top ($T_1$, $T_2$ and $T_3$) and bottom (B) fractions from a liposome PI3P(-) or PI3P(+) OptiprepTM co-floatation assay of His-VP3 FL protein (positive control, left panel) or His-VP3 ΔCt (right panel) showing the lack of VP3 ΔCt binding to both liposomes. Results are representative of three independent experiments. The bar plot represents the intensity of ($T_1$+$T_2$+$T_3$)/B bands for each liposome preparation. Significant differences (* $P$ <0.05; ns $P$ >0.05) as determined by one-way ANOVA with Tukey's HSD test.

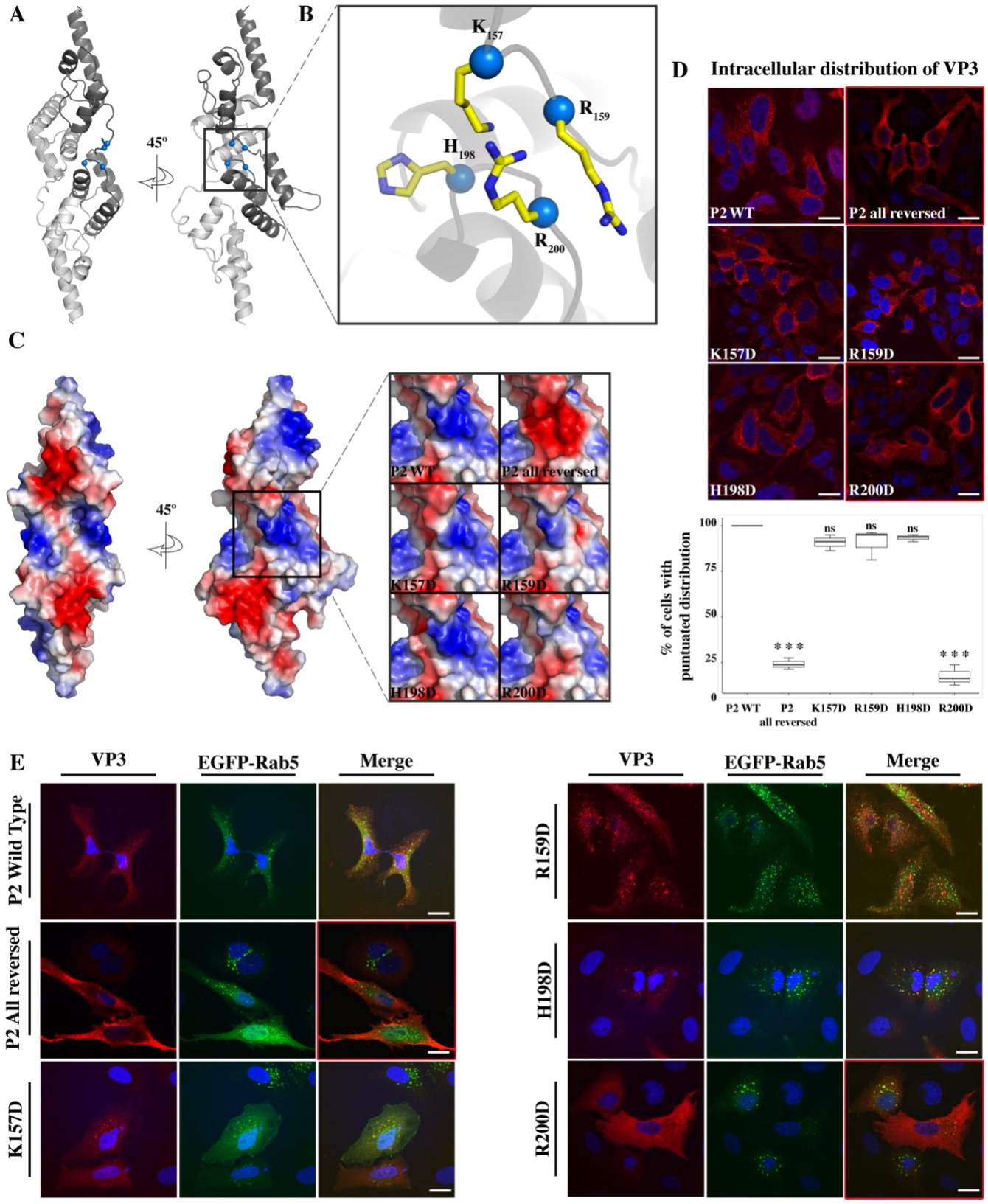
A
B
K157
R159
H198
R200
45°
C
P2 WT
P2 all reversed
K157D
R159D
H198D
R200D
D
Intracellular distribution of VP3
% of cells with puntuated distribution
ns
***
P2 WT
P2 all reversed
E
VP3
EGFP-Rab5
Merge
P2 Wild Type
P2 All reversed
K157D
R159D
H198D
R200D

**Figure 2. VP3 P2 involvement in the association of VP3 with the EE membrane.**

**(A)** The cartoon representation of the VP3 dimer [PDB 2R18 (Casañas et al., 2008)] shows each protomer in different shades of grey. The blue balls depict the residues defining the P2 region.

**(B)** The close-up of P2 region showing residues $K_{157}$, $R_{159}$, $H_{198}$ and $R_{200}$.

**(C)** Electrostatic potential mapped on the surface of the structure of a VP3 dimer in the same orientations as in (A) structures. The close-up shows the impact of P2 residue mutations on the electrostatic potential of the binding site. P2 WT corresponds to the "UniProt code". The color-coded electrostatic surface potential of VP3 was drawn using PyMol (blue positive, red negative).

**(D)** QM7 cells transfected with pcDNA VP3 FL (P2 WT), P2 (all reversed), or the four point mutants ($K_{157}D$, $R_{159}D$, $H_{198}D$ and $R_{200}D$) and immunostained with anti-VP3 showing the distribution of each protein (upper panel). Images were captured using a Confocal Laser Scanning Microscopy and then the percentage of cells with punctated fluorescent signal were determined for each protein (lower panel). The red signal shows the VP3 distribution and the blue one shows the nuclei, which were Hoestch-stained. The data were normalized to the P2 WT protein. The box plot represents the percentage of cells with punctuated distribution of VP3. Significant differences (*** $P$ <0.001; ns $P$ >0.05.) as determined by one-way ANOVA with Tukey's HSD test.

**(E)** QM7 cells co-transfected with pEGFP-Rab5 and pcDNA VP3 FL (P2 WT), P2 (all reversed), or the four point mutants ($K_{157}D$, $R_{159}D$, $H_{198}D$ and $R_{200}D$) and immunostained with anti-VP3 showing the distribution of each protein. Representative images, captured using a Confocal Laser Scanning Microscopy are shown where green signal represents Rab5 distribution and the red signal that of VP3. Nuclei were Hoestch-stained and are blue. White bar-scales represent 20 nm. VP3 P2 (all reversed) and $R_{200}D$ depict a cytosolic distribution of the proteins. Quantification of the co-localization of the different VP3 proteins and EGFP-Rab5 is shown in *SI Appendix*, Fig. S3.

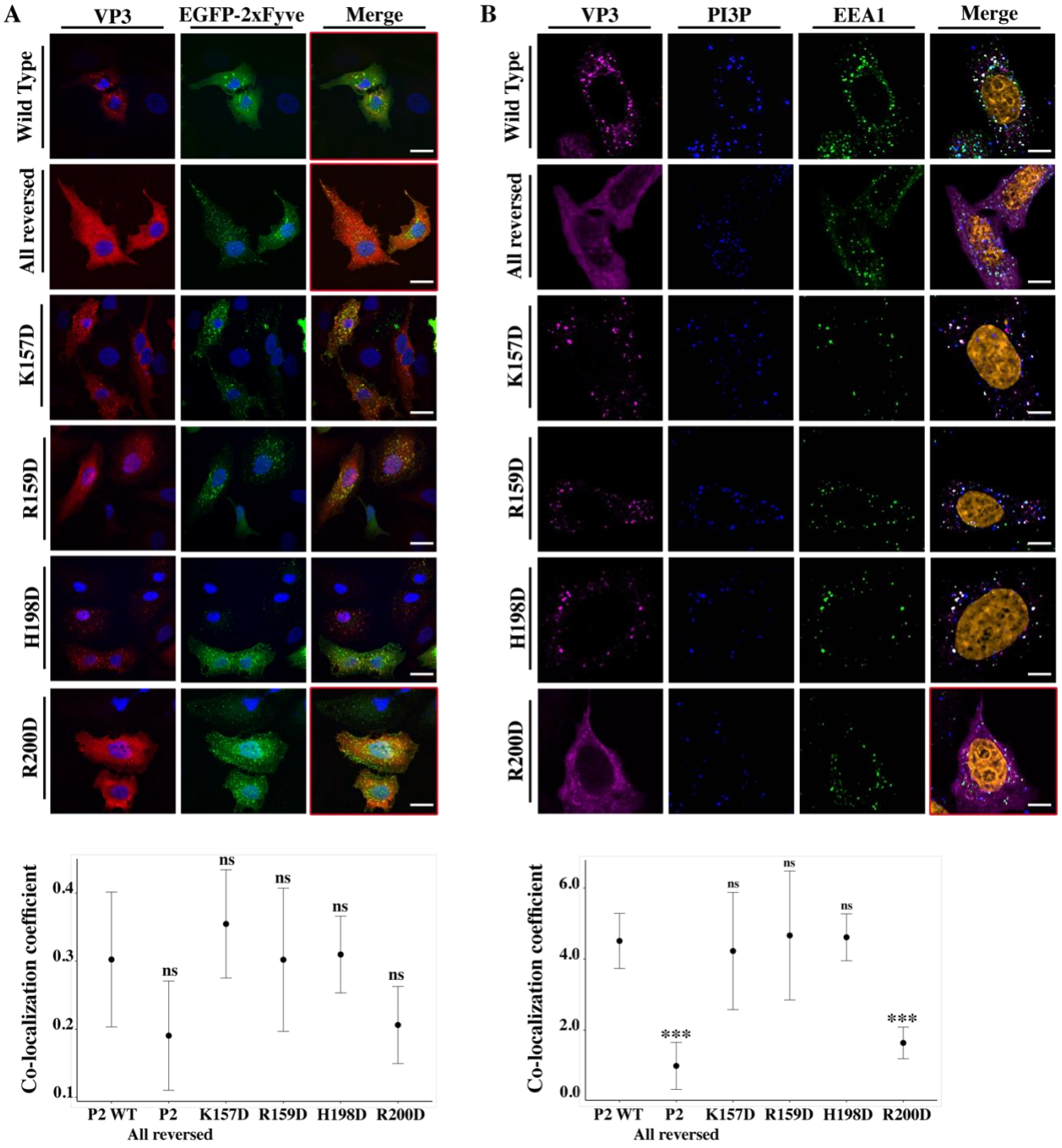


**Figure 3. VP3 P2 involvement in the association between VP3 and EE PI3P.**

**(A)** QM7 cells co-transfected with the PI3P biosensor pEGFP-2xFYVE and pcDNA VP3 FL (P2 WT), P2 (all reversed), or the four point mutants ($K_{157}D$, $R_{159}D$, $H_{198}D$ and $R_{200}D$) and immunostained with

anti-VP3 showing the distribution of each protein. Representative images, captured using a Confocal Laser Scanning Microscopy are shown where green signal represents FYVE distribution and the red signal that of VP3. Nuclei were Hoestch-stained and are blue (upper panel). White bar-scales represent 20 nm. VP3 P2 (all reversed) and $R_{200}D$ depict a cytosolic distribution of the proteins with a significant lower co-localization coefficient. The dot plot in the lower panel depicts the co-localization coefficient for each protein determined as explained in the Materials and Methods section. Significant differences (ns $P$ >0.05) as determined by one-way ANOVA with Tukey's HSD test.

**(B)** QM7 cells were transfected with the pcDNA VP3 FL (P2 WT), P2 (all reversed), or the four point mutants ($K_{157}D$, $R_{159}D$, $H_{198}D$ and $R_{200}D$). The cells were fixed and then the GST-2xFYVE purified peptide and anti-VP3 antibodies were used to recognize endogenous PI3P and VP3, respectively. Additionally anti-EEA1 antibodies were used to stain the endosomes. GST-2xFYVE was labelled with a fluorescent anti-GST antibody (blue signal), anti-VP3 and anti-EEA1 antibodies with fluorescent secondary antibodies (cyan and green signals, respectively), and Hoestch-stained nuclei in orange. White bar-scales represent 10 nm. VP3 P2 (all reversed) and $R_{200}D$ depict a cytosolic distribution of the proteins with a significant lower co-localization coefficient. The dot plot in the lower panel depicts the co-localization coefficient for each protein determined as explained in the Materials and Methods section. Significant differences (*** $P < 0.001$; ns $P$ >0.05) as determined by one-way ANOVA with Tukey's HSD test.

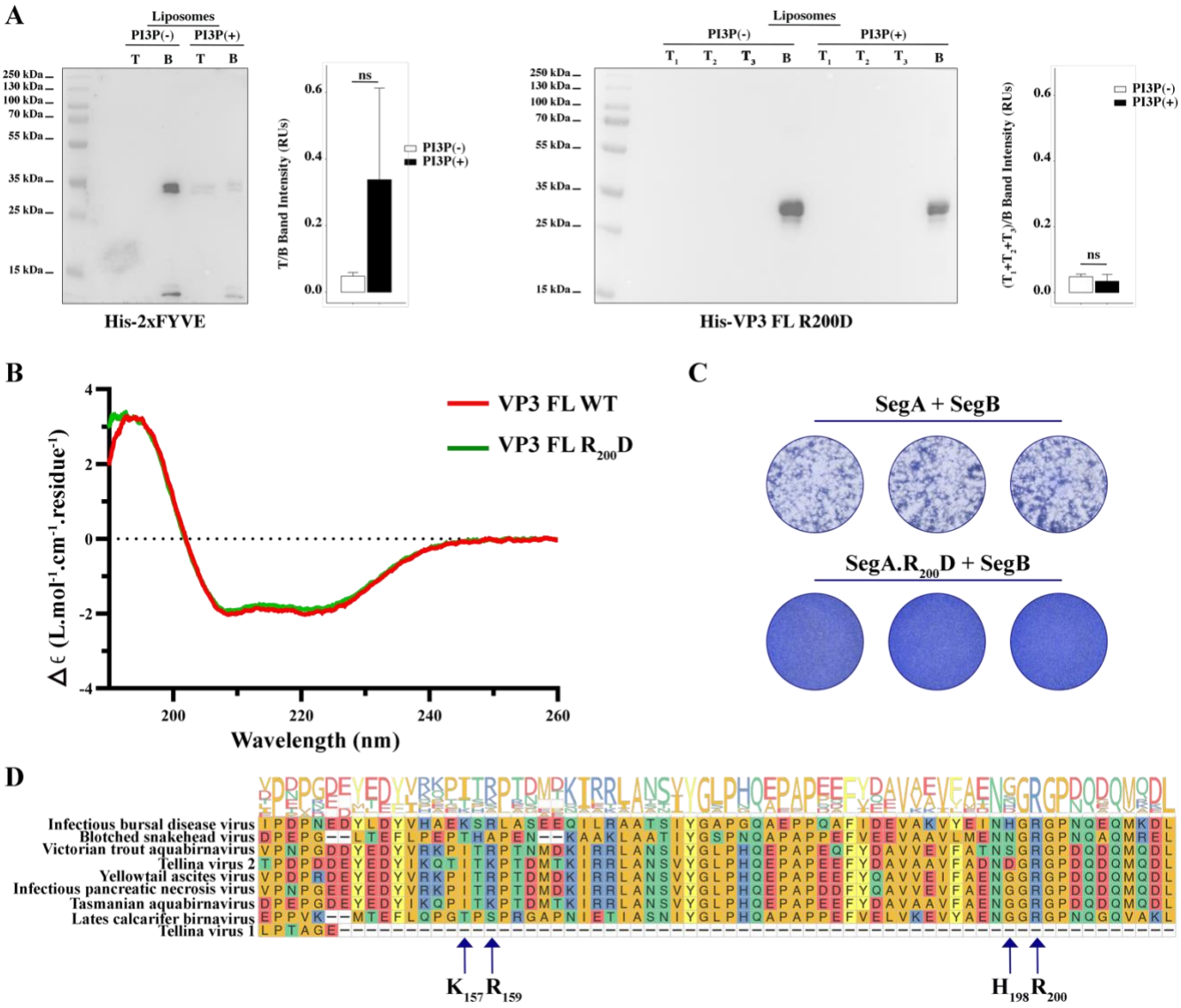


**Figure 4. Biophysical characterization of VP3 FL $R_{200}$D binding to PI3P.**

**(A, left panel)**. Immunoblots of the top (T) and bottom (B) fractions from a liposome PI3P(-) or PI3P(+) OptiprepTM co-floatation assay indicating that His-2xFYVE protein specifically binds to liposome PI3P(+). The bar plot represents the intensity of T/B bands for each liposome preparation. Significant differences (ns $P$ >0.05) as determined by one-way ANOVA with Tukey's HSD test.

**(A, rigth panel).** Immunoblots of the three top ($T_1$, $T_2$ and $T_3$) and bottom. (B) fractions from a liposome PI3P(-) or PI3P(+) OptiprepTM co-floatation assay indicating that His-VP3 FL $R_{200}$D does not bind to

liposome PI3P(-) nor PI3P(+). The bar plot represents the intensity of ($T_1$+$T_2$+$T_3$)/B bands for each liposome preparation. Significant differences (ns $P$ >0.05) as determined by one-way ANOVA with Tukey's HSD test.

**(B)** Far-UV CD spectra of His-VP3 FL (red line) or His-VP3 FL $R_{200}$D (green line). Spectral acquisitions at 50 nm/min with 0.1 nm steps at 1 s integration time, with a bandwidth of 1 nm were performed 4 times for the samples as well as for the buffer. The measurements were carried out with constant nitrogen gas flux of 10 ml/min. Acquisitions were averaged and buffer baseline was subtracted with Spectra Manager (JASCO). No smoothing was applied. CDtoolX was used to zero between 255-260 nm and to calibrate the signal amplitude from the fresh CSA signal (Miles and Wallace, 2018). Data are presented as delta epsilon ($\Delta\varepsilon$) per residue ($L.mol^{-1}.cm^{-1}.residue^{1}$) calculated using the molar concentration of protein and number of residues.

**(C)** QM7 cells were grown in M24 multi-well plate for 12 h to approximately 90-95% confluency and then 800 ng of plasmids were transfected [(SegA + SegB) or (SegA.$R_{200}$D + SegB)] in triplicate. At 8 h post-transfection (p.t.) the supernatants were discarded, and the monolayers were recovered for further plating on M6 multi-well plates containing non transfected QM7 cells. Avicel RC-591 (FMC Biopolymer) was added to the M6 multi-well plates. 72 h p.i., the monolayers were fixated and stained with Coomassie R250 for revealing the foci forming units.

**(D)** Partial view of amino acid alignment of the VP3 protein for nine reference members of *Birnaviridae* family. Multiple sequence alignment was performed with Clustal OMEGA (v1.2.4) (Sievers et al., 2011) implemented at EMBL's European Bioinformatics Institute ("EMBL's European Bioinformatics Institute," n.d.) (The complete alignment is shown in *SI Appendix*, Fig. S4A). Alignment visualization was done with the R *ggmsa* package (Zhou et al., 2022) in with assistance from the RStudio software (RStudio Team, 2020). Amino acids are colored according to their side-chain chemistry. Protein

sequence logos annotation is displayed on top of the amino acid alignment. For facilitating the view IBDV VP3 142-210 portion is shown. The black arrow indicates the $K_{157}$, $R_{159}$, $H_{198}$ and $R_{200}$.

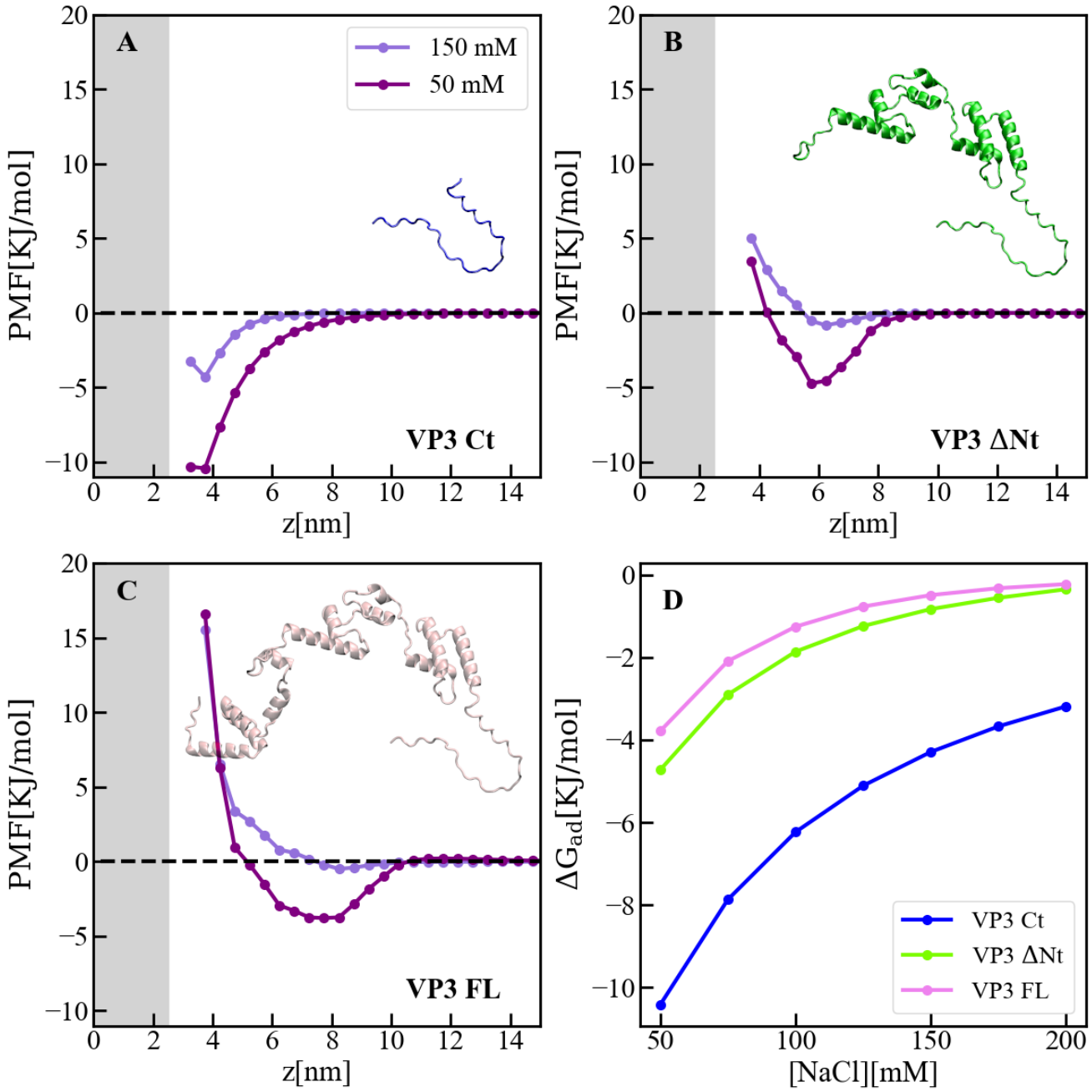


**Figure 5. Adsorption of VP3 constructs to PI3P(+) model membranes.**

**(A-C).** Adsorption free-energy profiles for VP3 Ct, VP3 Δ81 and VP3 FL at 50 and 150 mM of NaCl.

**(D)** Adsorption free energy ($\Delta G_{ad}$), computed from the minimum of PMF(z), versus concentration of NaCl. In all cases, the solution pH is 8, and the concentration of protein is 1 µM. The grey areas represent the volume excluded by half the membrane (cis hemilayer, z>0). The membrane surface contains 5% titratable groups, representing PI3P. Each group has three acidic moieties, one with a pKa of 2.5 and the others with 6.5. At 150 mM NaCl and pH 8, more than 90% of the acidic groups are deprotonated (*SI Appendix*, Fig. S5).

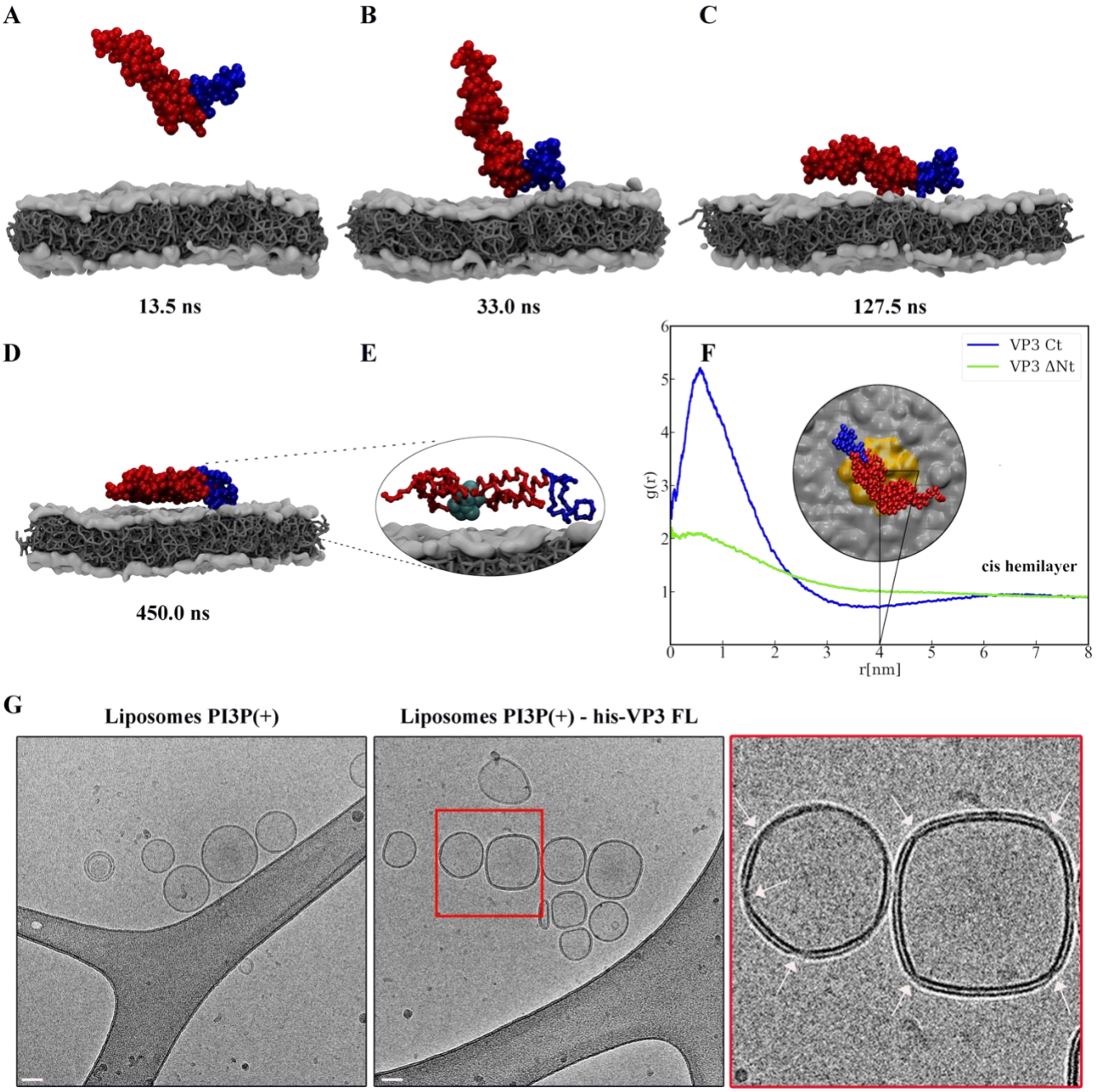


**Figure 6. VP3 approaching a lipid bilayer, and distortion of the membrane.**

**(A-D)** Temporal sequence of configurations illustrating how VP3 Δ81 approaches the negatively charged membrane during a 500 ns MD simulation. The membrane contains DOPE, DOPC and PI3P in 64:31:5 molar ratio. The beads making the Ct fragment are colored blue.

**(E)** Magnification of the protein configuration bound to the membrane, with P2 residues represented in cyan balls.

**(F)** Radial distribution function, g(r), between the center of mass of VP3 Δ81 and the center of PI3P molecules in the cis hemilayer. g(r) greater than 1 implies local enhancement of PI3P concentration. The inset shows an upper view of VP3 Δ81 bound to the membrane, with the area within r = 4 nm colored in light gray.

**(G)** Cryo-electron microscopy images of cryo-fixated liposomes PI3P(+) control (without protein, left panel), or incubated with His-VP3 FL showing the small pinches or localized thinnings in the bilayer of the liposomes when His-VP3 FL were present (middle panel). The bar represents 50 nm. The right panel represents an enlarged image of the red square on the middle panel. White arrows point the small pinches or localized thinnings in the bilayer of the liposomes when His-VP3 FL were present.

## References


AnalystSoft Inc., StatPlus:mac - v8. n.d.

Baltimore D. 1971. Expression of animal virus genomes. *Bacteriol Rev* **35**:235. doi:10.1128/BR.35.3.235-241.1971

Banani SF, Lee HO, Hyman AA, Rosen MK. 2017. Biomolecular condensates: organizers of cellular biochemistry. *Nat Rev Mol Cell Biol* **18**:285–298. doi:10.1038/NRM.2017.7

Bolte S, Cordelières FP. 2006. A guided tour into subcellular colocalization analysis in light microscopy. *J Microsc* **224**:213–232. doi:10.1111/j.1365-2818.2006.01706.x

Brodrick AJ, Broadbent AJ. 2023. The Formation and Function of Birnaviridae Virus Factories. *Int J Mol Sci* **24**. doi:10.3390/IJMS24108471

Casañas A, Navarro A, Ferrer-Orta C, González D, Rodríguez JF, Verdaguer N. 2008. Structural Insights into the Multifunctional Protein VP3 of Birnaviruses. *Structure* **16**:29–37. doi:10.1016/j.str.2007.10.023

Chiarpotti M V., Longo GS, Del Pópolo MG. 2021. Nanoparticles modified with cell penetrating peptides: Assessing adsorption on membranes containing acidic lipids. *Colloids Surf B Biointerfaces* **197**:111373. doi:10.1016/J.COLSURFB.2020.111373

Coulibaly F, Chevalier C, Gutsche I, Pous J, Navaza J, Bressanelli S, Delmas B, Rey FA. 2005. The birnavirus crystal structure reveals structural relationships among icosahedral viruses. *Cell* **120**:761–772. doi:10.1016/j.cell.2005.01.009

Darden T, York D, Pedersen L. 1993. Particle mesh Ewald: An N·log(N) method for Ewald sums in large systems. *J Chem Phys* **98**:10089–10092. doi:10.1063/1.464397

De Jong DH, Singh G, Bennett WFD, Arnarez C, Wassenaar TA, Schäfer L V., Periole X, Tieleman DP, Marrink SJ. 2013. Improved parameters for the martini coarse-grained protein force field. *J Chem Theory Comput* **9**:687–697. doi:10.1021/ct300646g

Delgui LR, Rodriguez JF, Colombo MI. 2013. The Endosomal Pathway and the Golgi Complex Are Involved in the Infectious Bursal Disease Virus Life Cycle. *J Virol* **87**:8993–9007. doi:10.1128/JVI.03152-12

Delmas B, Attoui H, Ghosh S, Malik YS, Mundt E, Vakharia VN. 2019. ICTV virus taxonomy profile: Birnaviridae. *Journal of General Virology* **100**:5–6. doi:10.1099/jgv.0.001185

EMBL's European Bioinformatics Institute. n.d. https://www.ebi.ac.uk/

F Olson, C A Hunt FCS, W J Vail DP. 1979. Preparation of liposomes of defined size distribution by extrusion through polycarbonate membranes. *Biochim Biophys Acta* **557**:9–23. doi:10.1016/0005-2736(79)90085-3

Fernandes F, Chen K, Ehrlich LS, Jin J, Chen MH, Medina GN, Symons M, Montelaro R, Donaldson J, Tjandra N, Carter CA. 2011. Phosphoinositides Direct Equine Infectious Anemia Virus Gag Trafficking and Release. *Traffic*. doi:10.1111/j.1600-0854.2010.01153.x

878 Ghanem A, Kern A, Conzelmann K-K. 2011. Significantly improved rescue of rabies virus from cDNA plasmids.
879 *Eur J Cell Biol* **91**:10–16. doi:10.1016/j.ejcb.2011.01.008

880 Gibson DG, Young L, Chuang R-Y, Venter JC, Hutchison CA 3rd, Smith HO. 2009. Enzymatic assembly of DNA
881 molecules up to several hundred kilobases. *Nat Methods* **6**:343–345. doi:10.1038/nmeth.1318

882 Gillooly DJ, Morrow IC, Lindsay M, Gould R, Bryant NJ, Gaullier JM, Parton RG, Stenmark H. 2000. Localization
883 of phosphatidylinositol 3-phosphate in yeast and mammalian cells. *EMBO Journal* **19**:4577–4588.
884 doi:10.1093/emboj/19.17.4577

885 Gimenez MC, Issa M, Sheth J, Colombo MI, Terebiznik MR, Delgui LR. 2020. Phosphatidylinositol 3-Phosphate
886 Mediates the Establishment of Infectious Bursal Disease Virus Replication Complexes in Association with
887 Early Endosomes. *J Virol* **95**:e02313-20. doi:10.1128/jvi.02313-20

888 Gimenez MC, Zanetti FA, Terebiznik MR, Colombo MI, Delgui LR. 2018. Infectious Bursal Disease Virus Hijacks
889 Endosomal Membranes as the Scaffolding Structure for Viral Replication. *J Virol* **92**:e01964-17.
890 doi:10.1128/JVI.01964-17

891 Gorbalenya AE, Pringle FM, Zeddam JL, Luke BT, Cameron CE, Kalmakoff J, Hanzlik TN, Gordon KHJ, Ward VK.
892 2002. The palm subdomain-based active site is internally permuted in viral RNA-dependent RNA
893 polymerases of an ancient lineage. *J Mol Biol* **324**:47–62. doi:10.1016/S0022-2836(02)01033-1

894 Gorvel JP, Chavrier P, Zerial M, Gruenberg J. 1991. rab5 controls early endosome fusion in vitro. *Cell* **64**:915–25.

895 Johnson WC. 1999. Analyzing Protein Circular Dichroism Spectra for Accurate Secondary Structures. *Proteins*
896 **35**:307–312. doi:10.1002/(SICI)1097-0134(19990515)35:3

897 Jumper J, Evans R, Pritzel A, Green T, Figurnov M, Ronneberger O, Tunyasuvunakool K, Bates R, Žídek A,
898 Potapenko A, Bridgland A, Meyer C, Kohl SAA, Ballard AJ, Cowie A, Romera-Paredes B, Nikolov S, Jain R,
899 Adler J, Back T, Petersen S, Reiman D, Clancy E, Zielinski M, Steinegger M, Pacholska M, Berghammer T,
900 Bodenstein S, Silver D, Vinyals O, Senior AW, Kavukcuoglu K, Kohli P, Hassabis D. 2021. Highly accurate
901 protein structure prediction with AlphaFold. *Nature 2021 596:7873* **596**:583–589. doi:10.1038/s41586-
902 021-03819-2

903 JustBio. n.d.

904 Kairys V, Baranauskiene L, Kazlauskiene M, Matulis D, Kazlauskas E. 2019. Binding affinity in drug design:
905 experimental and computational techniques. *https://doi.org/101080/1746044120191623202* **14**:755–
906 768. doi:10.1080/17460441.2019.1623202

907 Kolli S, Meng X, Wu X, Shengjuler D, Cameron CE, Xiang Y, Deng J. 2015. Structure-Function Analysis of Vaccinia
908 Virus H7 Protein Reveals a Novel Phosphoinositide Binding Fold Essential for Poxvirus Replication. *J Virol*
909 **89**:2209–2219. doi:10.1128/JVI.03073-14/ASSET/F1575F5D-784E-4FD0-9DDB-
910 A2B374935CCA/ASSETS/GRAPHIC/ZJV9990900510007.JPEG

911 Komada M, Kitamura N. 1995. Growth factor-induced tyrosine phosphorylation of Hrs, a novel 115-kilodalton
912 protein with a structurally conserved putative zinc finger domain. *Mol Cell Biol* **15**:6213–6221.
913 doi:10.1128/MCB.15.11.6213

914 Koonin E V., Dolja V V., Krupovic M, Varsani A, Wolf YI, Yutin N, Zerbini FM, Kuhn JH. 2020. Global Organization
915 and Proposed Megataxonomy of the Virus World. *Microbiology and Molecular Biology Reviews* **84**.
916 doi:10.1128/MMBR.00061-19/SUPPL_FILE/MMBR.00061-19-S0001.PDF

917 Lees JG, Miles AJ, Wien F, Wallace BA. 2006. A reference database for circular dichroism spectroscopy covering
918 fold and secondary structure space. *Bioinformatics* **22**:1955–1962. doi:10.1093/BIOINFORMATICS/BTL327

919 Lombardo E, Maraver A, Castón JR, Rivera J, Fernández-Arias A, Serrano A, Carrascosa JL, Rodriguez JF. 1999.
920 VP1, the putative RNA-dependent RNA polymerase of infectious bursal disease virus, forms complexes
921 with the capsid protein VP3, leading to efficient encapsidation into virus-like particles. *J Virol* **73**:6973–83.

922 Luque D, Rivas G, Alfonso C, Carrascosa JL, Rodríguez JF, Castón JR. 2009a. Infectious bursal disease virus is an
923 icosahedral polyploid dsRNA virus. *Proc Natl Acad Sci U S A* **106**:2148–52. doi:10.1073/pnas.0808498106

924 Luque D, Saugar I, Rejas MT, Carrascosa JL, Rodríguez JF, Castón JR. 2009b. Infectious Bursal Disease Virus:
925 Ribonucleoprotein Complexes of a Double-Stranded RNA Virus. *J Mol Biol* **386**:891–901.
926 doi:10.1016/j.jmb.2008.11.029

927 Marrink SJ, Risselada HJ, Yefimov S, Tieleman DP, De Vries AH. 2007. The MARTINI force field: Coarse grained
928 model for biomolecular simulations. *Journal of Physical Chemistry B* **111**:7812–7824.
929 doi:10.1021/jp071097f

930 Matsuda T, Cepko CL. 2004a. Electroporation and RNA interference in the rodent retina in vivo and in vitro.
931 *Proc Natl Acad Sci U S A* **101**:16–22. doi:10.1073/pnas.2235688100

932 Matsuda T, Cepko CL. 2004b. Electroporation and RNA interference in the rodent retina in vivo and in vitro.
933 *Proc Natl Acad Sci U S A* **101**:16–22. doi:10.1073/PNAS.2235688100

934 Mcnulty S, Bornmann W, Schriewer J, Werner C, Smith SK, Olson VA, Damon IK, Buller RM, Heuser J, Kalman D.
935 2010. Multiple Phosphatidylinositol 3-Kinases Regulate Vaccinia Virus Morphogenesis. *PLoS One*
936 **5**:e10884. doi:10.1371/JOURNAL.PONE.0010884

937 Miles AJ, Wallace BA. 2018. CDtoolX, a downloadable software package for processing and analyses of circular
938 dichroism spectroscopic data. *Protein Science* **27**:1717–1722. doi:10.1002/pro.3474

939 Nascimbeni AC, Codogno P, Morel E. 2017. Local detection of PtdIns3P at autophagosome biogenesis
940 membrane platforms. *Autophagy* **13**:1602–1612. doi:10.1080/15548627.2017.1341465

941 Parrinello M, Rahman A. 1981. Polymorphic transitions in single crystals: A new molecular dynamics method. *J*
942 *Appl Phys* **52**:7182–7190. doi:10.1063/1.328693

943 Periole X, Cavalli M, Marrink SJ, Ceruso MA. 2009. Combining an elastic network with a coarse-grained
944 molecular force field: Structure, dynamics, and intermolecular recognition. *J Chem Theory Comput*
945 **5**:2531–2543. doi:10.1021/CT9002114/SUPPL_FILE/CT9002114_SI_001.PDF

946 Poma AB, Cieplak M, Theodorakis PE. 2017. Combining the MARTINI and Structure-Based Coarse-Grained
947 Approaches for the Molecular Dynamics Studies of Conformational Transitions in Proteins. *J Chem Theory*
948 *Comput* **13**:1366–1374. doi:10.1021/ACS.JCTC.6B00986/ASSET/IMAGES/LARGE/CT-2016-
949 00986K_0005.JPEG

950 Potgieter AC, Page NA, Liebenberg J, Wright IM, Landt O, van Dijk AA. 2009. Improved strategies for sequence-
951 independent amplification and sequencing of viral double-stranded RNA genomes. *J Gen Virol* **90**:1423–
952 1432. doi:10.1099/vir.0.009381-0

953 Provencher SW, Glöckner J. 1981. Estimation of Globular Protein Secondary Structure from Circular Dichroism.
954 *Biochemistry* **20**:33–37. doi:10.1021/bi00504a006

955 Puffer BA, Watkins SC, Montelaro RC. 1998. Equine infectious anemia virus Gag polyprotein late domain
956 specifically recruits cellular AP-2 adapter protein complexes during virion assembly. *J Virol* **72**:10218–
957 10221. doi:10.1128/JVI.72.12.10218-10221.1998

958 Qi X, Gao Y, Gao H, Deng X, Bu Z, Wang Xiaoyan, Fu C, Wang Xiaomei. 2007. An improved method for infectious
959 bursal disease virus rescue using RNA polymerase II system. *J Virol Methods* **142**:81–88.
960 doi:10.1016/j.jviromet.2007.01.021

961 Ramírez PG, Del Pópolo MG, Vila JA, Szleifer I, Longo GS. 2019. Adsorption and insertion of polyarginine
962 peptides into membrane pores: The trade-off between electrostatics, acid-base chemistry and pore
963 formation energy. *J Colloid Interface Sci* **552**:701–711. doi:10.1016/J.JCIS.2019.05.087

964 Reddy V, Lymar E, Hu M, Hainfeld JF. 2005. 5 nm Gold-Ni-NTA Binds His Tags. *Microscopy and Microanalysis*
965 **11**:1118–1119. doi:10.1017/S1431927605507712

966 Reddy VRAP, Campbell EA, Wells J, Simpson J, Nazki S, Hawes PC, Broadbent AJ. 2022. Birnaviridae Virus
967 Factories Show Features of Liquid-Liquid Phase Separation and Are Distinct from Paracrystalline Arrays of
968 Virions Observed by Electron Microscopy. *J Virol* **96**:e0202421. doi:10.1128/jvi.02024-21

969 RStudio Team. 2020. RStudio: Integrated Development Environment for R.

970 Rydzanicz R, Zhao XS, Johnson PE. 2005. Assembly PCR oligo maker: a tool for designing oligodeoxynucleotides
971 for constructing long DNA molecules for RNA production. *Nucleic Acids Res* **33**:W521-5.
972 doi:10.1093/nar/gki380

973 Saugar I, Irigoyen N, Luque D, Carrascosa JL, Rodríguez JF, Castón JR. 2010. Electrostatic interactions between
974 capsid and scaffolding proteins mediate the structural polymorphism of a double-stranded RNA virus. *J*
975 *Biol Chem* **285**:3643–50. doi:10.1074/jbc.M109.075994

976 Schindelin J, Arganda-Carreras I, Frise E, Kaynig V, Longair M, Pietzsch T, Preibisch S, Rueden C, Saalfeld S,
977 Schmid B, Tinevez J-Y, White DJ, Hartenstein V, Eliceiri K, Tomancak P, Cardona A. 2012. Fiji: an open-
978 source platform for biological-image analysis. *Nat Methods* **9**:676–682. doi:10.1038/nmeth.2019

979 Shah NB, Duncan T, M. 2014. Bio-layer interferometry for measuring kinetics of protein-protein interactions
980 and allosteric ligand effects. *J Vis Exp*. doi:10.3791/51383

981 Sievers F, Wilm A, Dineen D, Gibson TJ, Karplus K, Li W, Lopez R, McWilliam H, Remmert M, Söding J, Thompson
982 JD, Higgins DG. 2011. Fast, scalable generation of high-quality protein multiple sequence alignments using
983 Clustal Omega. *Mol Syst Biol* **7**:539. doi:10.1038/MSB.2011.75

984 Sreerama N, Woody RW. 2000. Estimation of protein secondary structure from circular dichroism spectra:
985 Comparison of CONTIN, SELCON, and CDSSTR methods with an expanded reference set. *Anal Biochem*
986 **287**:252–260. doi:10.1006/abio.2000.4880

987 Tanzi GO, Piefer AJ, Bates P. 2003. Equine infectious anemia virus utilizes host vesicular protein sorting
988 machinery during particle release. *J Virol* **77**:8440–8447. doi:10.1128/JVI.77.15.8440-8447.2003

989 Valli A, Busnadiego I, Maliogka V, Ferrero D, Castón JR, Rodríguez JF, García JA. 2012. The VP3 Factor from
990 Viruses of Birnaviridae Family Suppresses RNA Silencing by Binding Both Long and Small RNA Duplexes.
991 *PLoS One* **7**:e45957. doi:10.1371/journal.pone.0045957

992 Walker PJ, Siddell SG, Lefkowitz EJ, Mushegian AR, Adriaenssens EM, Alfenas-Zerbini P, Davison AJ, Dempsey
993 DM, Dutilh BE, García ML, Harrach B, Harrison RL, Hendrickson RC, Junglen S, Knowles NJ, Krupovic M,
994 Kuhn JH, Lambert AJ, Łobocka M, Nibert ML, Oksanen HM, Orton RJ, Robertson DL, Rubino L,
995 Sabanadzovic S, Simmonds P, Smith DB, Suzuki N, Van Dooerslaer K, Vandamme AM, Varsani A, Zerbini
996 FM. 2021. Changes to virus taxonomy and to the International Code of Virus Classification and
997 Nomenclature ratified by the International Committee on Taxonomy of Viruses (2021). *Arch Virol*
998 **166**:2633–2648. doi:10.1007/S00705-021-05156-1

999 Wassenaar TA, Ingólfsson HI, Böckmann RA, Tieleman DP, Marrink SJ. 2015. Computational lipidomics with
1000 insane: A versatile tool for generating custom membranes for molecular simulations. *J Chem Theory*
1001 *Comput* **11**:2144–2155. doi:10.1021/acs.jctc.5b00209

1002 Whitmore L, Wallace BA. 2008. Protein secondary structure analyses from circular dichroism spectroscopy:
1003 Methods and reference databases. *Biopolymers* **89**:392–400. doi:10.1002/bip.20853

1004 Whitmore L, Wallace BA. 2004. DICHROWEB, an online server for protein secondary structure analyses from
1005 circular dichroism spectroscopic data. *Nucleic Acids Res* **32**. doi:10.1093/nar/gkh371

1006 Wickham H. 2016. ggplot2: Elegant Graphics for Data Analysis. Springer-Verlag New York.

1007 Wills JW, Craven RC. 1991. Form, function, and use of retroviral gag proteins. *AIDS* **5**:639–654.
1008 doi:10.1097/00002030-199106000-00002

1009 Wolf YI, Kazlauskas D, Iranzo J, Lucía-Sanz A, Kuhn JH, Krupovic M, Dolja V V., Koonin E V. 2018. Origins and
1010 Evolution of the Global RNA Virome. *mBio* **9**. doi:10.1128/MBIO.02329-18

1011 Yanai H, Hayashi Y, Watanabe Y, Ohtaki N, Kobayashi T, Nozaki Y, Ikuta K, Tomonaga K. 2006. Development of a
1012 novel Borna disease virus reverse genetics system using RNA polymerase II promoter and SV40 nuclear
1013 import signal. *Microbes Infect* **8**:1522–1529. doi:10.1016/j.micinf.2006.01.010

1014 Zhou L, Feng T, Xu S, Gao F, Lam TT, Wang Q, Wu T, Huang H, Zhan L, Li L, Guan Y, Dai Z, Yu G. 2022. ggmsa: a
1015 visual exploration tool for multiple sequence alignment and associated data. *Brief Bioinform* **23**.
1016 doi:10.1093/BIB/BBAC222

1017